ULTRAFAST PHONON AND SPIN DYNAMICS STUDIES IN MAGNETIC HETEROSTRUCTURE SYSTEMS

By

Jingbo Qi

Dissertation

Submitted to the faculty of the

Graduate school of Vanderbilt University

in partial satisfaction of the requirements

for the degree of

DOCTOR OF PHILOSOPHY

in

Physics

December 2008

Nashville, Tennessee

Approved:

Professor Norman H. Tolk

Professor Daniel M. Fleetwood

Professor Thomas W. Kephart

Professor Kalman Varga

Professor Ilias E. Perakis

To my parents for their love and support.

ACKNOWLEDGEMENTS

I have spent a wonderful time during my stay at Vanderbilt as a Ph.D. graduate student. It is a great pleasure to express my gratitude to those with whom I have interacted during my graduate student years.

First of all, I would like to thank very much my supervisor Norman Tolk. His enthusiasm towards science is always inspiring to me. His patience and knowledge has been an essential element in completing this work. Without his support, not only in science and technology but also in my personal life in Nashville, I could never have learned so much or progressed as rapidly during my Ph.D. studies. I have benefited tremendously from the many opportunities he has given to me.

I would like to express my thanks to all the members of my committee: Daniel Fleetwood, Thomas Kephart, Kalman Varga, and Ilias Perakis for their valuable comments and suggestions in this work. Especially, Ilias has given me substantial help on theoretically understanding and modeling coherent spin dynamics, which is one of the essential parts of my dissertation.

The CMASS group I have been working is a wonderful group, in which there are so many nice people, and talented youngsters. I particulary thank Ying Xu for her help in the experiments. Ying showed me the essentials of how to make a very successful pump-probe setup, and how to efficiently tune and align the ultrafast laser systems. Discussions with her are always stimulating and inspiring. I thank the past member of our group, Keith Miller, for his first detail demonstration on how to perform low temperature measurements using liquid nitrogen and liquid helium. This helped me very much during my later personal independent measurements employing low temperature techniques. I thank Andrew Steigerwald for his depositing metal films on my studies samples, and the help he provided when I performed my experiments. I also thank all the other past and present members in this group, especially Xiong Lu, Travis Wade, Heungman Park, Justin Gregory, and Jane Fall. All of the above members contributed to my success.

Many thanks go to the MBE group in University of Notre Dame: Jacek Furdyna and Xinyu Liu. I really appreciate them for providing really high quality GaMnAs films! In particular, discussions with Xinyu improve my understanding of the physics of low temperature growth techniques.

I would also like to thank my friends in Nashville, especially my Chinese friends. Without them, my time at Vanderbilt University would not have been as enjoyable.

Finally, I would like to thank my parents, brother, and Nan for always being supportive of me and my decisions, and for their love and encouragement.

TABLE OF CONTENTS

Page

LIST OF TABLES

LIST OF FIGURES

CHAPTER I

INTRODUCTION

1.1 Perspective

Since the discovery of giant magnetoresistance (GMR) resulting in the awarding of a Nobel Prize [1, 2], the spin of the electron has attracted significant interest in the field of microelectronics. Spintronics (spin-based electronics or magnetoelectronics), which involves manipulating both quantum spin states of electrons and their charge states, promises a wide variety of applications in storage, logic and sensors. The fact that spintronics research may lead to quantum computers, quantum cryptography, and quantum communications in the not so distant future, has excited the imagination of many researchers [3, 4]. In order to integrate spintronic devices into conventional semiconductor technology, it will be necessary to obtain an enhanced understanding of both theory and experiment related to the rich phenomena associated with the spin degree freedom for electrons in ferromagnetic materials and semiconductors [5]. Recent developments in epitaxial thin film growth techniques, especially the state-of-the-art control of doping and of the magnitude of the bandgap of semiconductors, provide unique opportunities to carry out spin-related experiments wherein one may manipulate spin interactions by optical, electrical and magnetic methodologies. The basic thrust of this dissertation encompasses three major topics: 1) carrier and phonon ultrafast dynamics; 2) optically excited spin coherence in the diluted magnetic semiconductor (Ga,Mn)As system; and 3) variation in the magnetic properties of the ferromagnetic/antiferromagnetic Fe/NiO system as a function of the thickness of the ferromagnetic layer.

1.2 Background

Controlling coherent spins locally or nonlocally in magnetic and nonmagnetic materials by a variety of different methodologies is the most challenging issue in spintronics [4, 6]. Important concerns in both experiment and theory include optimization of

coherent spin lifetimes, detection of spin coherence in nanostructures, transport of spin-polarized current through appropriate length scales and across heterostructures, and the manipulation of both carrier and nuclear spins on ultrafast time scales [3]. Much effort has been expended in this direction. Here we address some contemporary research efforts in this field, which are particularly relevant and promising. Recent time-resolved magneto-optic spectroscopy in nonmagnetic GaAs shows that the coherent spin lifetime of conduction electrons is relatively long compared to typical semiconductors and metals [7, 8], which now makes it possible to transport coherent spin polarized electrons more than 100 microns [9, 10]. In experiments motivated by quantum computing, nuclear magnetic resonance, employing a combination of static and radio-frequency magnetic fields, was shown to be an effective approach for the manipulation of nuclear spins [11]. Gigahertz electron spin manipulation by electrical gated control has been demonstrated in GaAs-based semiconductor heterostructures [12, 13]. Recent experiments demonstrate that ultrafast laser pulses on magnetically ordered non-semiconductor materials can lead to demagnetization [14, 15, 16, 17, 18, 19, 20], spin-reorientation [21, 22], or change of magnetic structure [23]. The authors attributed these observations to either a laser heating effect or to a nonthermal inverse Faraday effect [24]. Over the past few decades much work has been devoted to combining the robust properties of both semiconductor and magnetic materials, with emphasis on diluted magnetic semiconductors (DMSs). A much studied example of diluted magnetic semiconductor is manganese doped gallium arsenide (Ga, Mn)As. Since this material is characterized by strongly carrier-mediated ferromagnetism, the magnetic properties may be controlled electrically, optically or by other external means [25, 26]. A major motivation in these studies is the desire to realize high temperature ferromagnetism [27, 28], which is supremely important for future technologies.

1.3 Organization

This dissertation is organized as follows. Chapter 2 deals with the fundamentals of magneto-optics and introduces the experimental configuration. In chapter 3, a brief discussion and review of (III,Mn)V diluted magnetic semiconductors is presented. Chapter 4 presents results of experimental studies of propagating coherent acoustic phonon dynamics [29] and magnetization dynamics [30, 31, 32] in (Ga,Mn)As systems. Chapter 5 describes magnetism-induced second harmonic generation measurements on ferromagnetic/antiferromagnetic Fe/NiO system [33]. Finally, Chapter 6 provides comments and conclusions.

CHAPTER II

MAGNETO OPTICS

2.1 Introduction

Magneto-optics is a very important and useful tool for the study of spin related phenomena involving the interaction of light and magnetically ordered matter (ferromagnets) or non-magnetic materials(semiconductors) [34, 35]. The presence of ordered spins in a material changes the dispersion curves of the absorption coefficient and results in either the emergence of, or a change in, optical anisotropy. The optical anisotropy of a magnetized material manifests itself both in the transmission of light through its bulk and in the reflection of the light from its surface. It has been shown experimentally that linearly polarized light experiences a rotation of its polarization state with propagation through or reflection from a magnetic medium, as long as the propagation direction has a component parallel to the magnetization **M**. This effect in transmission and reflection is generally referred to as the magneto-optical Faraday effect [36] and the magneto-optical Kerr effect(MOKE) [37], respectively. The complex rotation $\Theta_K = \theta + i\varepsilon$ corresponds to a true rotation of the polarization by an angle θ and an introduced ellipticity of ε. In addition to linear MOKE, non-linear magneto-optical approaches, in particular, magnetism-induced second harmonic generation (MSHG) [38, 39], are becoming increasingly important because they are non-destructive and also surface and interface sensitive. In some cases, non-linear MOKE produces a much-enhanced signal in comparison with linear MOKE. When the incident laser pulse widths are of the order of a picosecond or less, these magneto-optical effects can in particular reveal direct time domain information about the magnetic properties of excited states with high spatial and temporal resolution. Time-resolved magneto-optical spectroscopy has already enabled enhanced understanding of spin relaxation, coherence and decoherence effects in semiconductors and their quantum confined structures. It is clear, however, that much needs yet to accomplished in order

to realize the full potential of these approaches to the field of semiconductor-based spintronics [4, 40, 41, 42].

2.2 Faraday Rotation and Magneto-optical Kerr Effect (MOKE)

Phenomenologically, the complex Faraday rotation of the polarization plane after traveling a distance L in the medium is given by [34]

$$\Theta_F = \pi L(n_L - n_R)/\lambda \cong -\frac{L\pi n_0}{\lambda}Q, \tag{2.1}$$

where n_L and n_R are the refractive indices of left circular polarized and right circular polarized light, respectively. Q is the magneto-optical parameter, which is usually proportional to the magnetization under first order approximation.

Depending on the direction of the magnetization, three types of MOKE effects are generally distinguished (see Figure 2.1): longitudinal, polar, and transverse Kerr effects. The presence of the rotation of polarization plane is a general feature of the polar and longitudinal Kerr effects because of the non-zero projection of the wave vector **k** of the electromagnetic wave in the magnetization direction. Therefore, in the transverse geometry, the light reflected by the magnetic medium reveals the change of intensity and phase of the incident linearly polarized light only. The general formulae for the magneto-optical Kerr effects take the following forms [34]:

(I) the polar Kerr effect:

$$\Theta_K^{s,p} = \frac{\eta^2[(\eta^2 - \sin^2(\phi))^{1/2} \mp \sin(\phi)\tan(\phi)]}{(\eta^2 - 1)(\eta^2 - \tan^2(\phi))}Q, \tag{2.2}$$

(II) the longitudinal Kerr effect:

$$\Theta_K^{s,p} = \frac{\sin(\phi)\eta^2[\sin(\phi)\tan(\phi) \pm \sqrt{\eta^2 - \sin^2(\phi)}]}{(\eta^2 - 1)(\eta^2 - \tan^2(\phi))(\eta^2 - \sin^2(\phi))^{1/2}}Q, \tag{2.3}$$

(III) the transverse Kerr effect:

$$\Delta_p = \frac{\Delta I}{I} = \frac{-4\tan(\phi)\eta^2}{(\eta^2 - 1)(\eta^2 - \tan^2(\phi))}Q. \tag{2.4}$$

Here $\Theta_K^{s,p}$, where the upper signs s(or p) corresponds to s(or p) polarization of light, is the complex Kerr rotation. $\eta = n_2/n_1$ is the complex relative refractive index of the adjacent media. ϕ is the angle of the incident light. Q is the magneto-optical parameter. I is the intensity of the reflected beam.

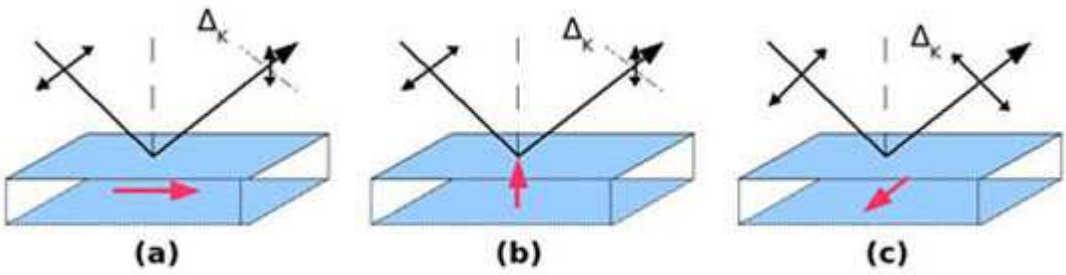

Figure 2.1: Three configurations of MOKE effect: (a) Longitudinal; (b)Polar; (c) Transverse. Here, red arrow represents the direction of magnetization.

2.3 Magnetism-induced Second Harmonic Generation (MSHG)

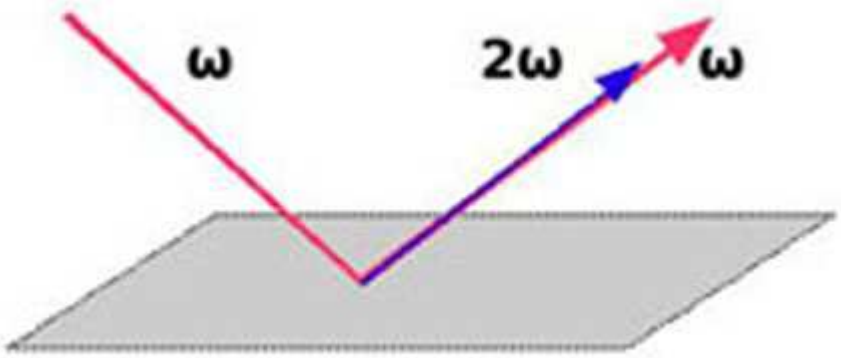

Figure 2.2: Second Harmonic Generation is generated at an interface of two centrosymmetric media, in this case: air/ sample.

Second harmonic generation (SHG) [43, 44] is a process that involves quadratic polarization where only a single monochromatic electromagnetic field with frequency

ω is incident. A field with frequency ω propagates in a nonlinear crystal and generates a polarization wave with frequency 2ω. This polarization induces an electric field with frequency 2ω (blue light, a so-called second harmonic wave) in the nonlinear medium (Figure 2.2). Therefore, the second harmonic generation can be described by the second term in following equation [43, 44]

$$\mathbf{P} = \chi^{(1)}\mathbf{E} + \chi^{(2)}\mathbf{EE} + \chi^{(3)}\mathbf{EEE} + \cdots , \tag{2.5}$$

where $\chi^{(n)}$ is the susceptibility tensor of n-th order and rank n+1. Hence, we can represent second harmonic polarization as $P_i(2\omega) = \chi^{(2)}_{ijk} E_j(\omega) E_k(\omega)$. This third rank tensor consists of 27 elements. In a single beam experiment, the indices j and k are interchangeable. Thus the number of independent of elements is reduced to 18. For centrosymmetric (equivalent to three orthogonal mirror transformation) media, there is no second harmonic generation contribution from the bulk. Because this symmetry is broken at the surface/interface, non-zero susceptibility tensor components appear, which leads to surface/interface induced second harmonic generation.

Introducing magnetization into the centrosymmetric magnetic media does not usually break the inversion symmetry except for the magneto-electrical material [45], where an electric field can induce change in magnetization and an external magnetic field can induce electric polarization. But it can modify the form of the non-linear susceptibility for surface/interface derived SHG. This results in the addition of an new term referred to as magnetism-induced second harmonic generation (MSHG). MSHG is very similar to MOKE. In MSHG, the presence of magnetization $\mathbf{M}$ in the sample will cause a rotation of the polarization plane (longitudinal and polar components of $\mathbf{M}$) and intensity changes (transverse component of $\mathbf{M}$). Second harmonic magneto-optical Kerr effect (SHMOKE) is also a frequently used name for MSHG. For crystals with a spontaneous or magnetic field induced magnetization $\mathbf{M}$, the nonlinear second order optical polarization of a medium can be written as $\mathbf{P}^{nl}(2\omega) = \chi^{cr}\mathbf{E}(\omega)\mathbf{E}(\omega) + \chi^{magn}(\mathbf{M})\mathbf{E}(\omega)\mathbf{E}(\omega)$, or simplified to $\mathbf{P}^{nl}(2\omega) = \chi^{(2)}(\mathbf{M})\mathbf{E}(\omega)\mathbf{E}(\omega)$, where the third rank tensor component $\chi^{(2)}$ is either even or odd in $\mathbf{M}$ [39, 46]. So, the introduction

of a magnetization **M** leads to susceptibility tensor components $\chi^{(2)}$ that do not change sign (even), that change sign (odd) with respect to **M** or that only include the crystallographic contribution. Given that the material is centrosymmetric or possesses inversion symmetry, detailed expressions for the surface/interface tensor components for the (001) and (110) surfaces of fcc crystals are listed in the following tables 2.1 and 2.2, respectively [46]. The MSHG intensity, to within a scaling factor, can be expressed as:

$$I(2\omega, M_L) = |\chi^{eff}_{even}|^2 + |\chi^{eff}_{odd}(M_L)|^2 + 2|\chi^{eff}_{even}||\chi^{eff}_{odd}(M_L)|cos\delta, \tag{2.6}$$

where χ^{eff}_{even} is the effective crystallographic term, χ^{eff}_{odd} is the effective magnetic term, M_L is the component of the magnetization along L, and δ is the phase difference between the even crystallographic and the odd magnetic contribution [47]. The term $\chi^{eff}_{odd}(M_L)$ is proportional to the magnetization. The Fresnel factors are already included in the effective tensor components. Hysteresis loops may be acquired by varying the external magnetic field. Usually, the third rank crystallographic tensor components are also expressed using the short-hand notation $\chi_{ijk} \equiv ijk$, while the fourth rank magnetic tensor components are expressed as $\chi_{ijkL} \equiv ijkL$, where the upper-case subscript L describes the magnetization direction.

2.4 Time-resolved Magneto-optics

A typical time-resolved MOKE(TRMOKE) or Faraday rotation (TRFR) setup always employs a pump-probe scheme, where femtosecond pump and probe pulses are focused on overlapping spots on the sample to be studied. The time duration between the probe pulse and the pump pulse incident on the sample can be varied with a mechanical translation stage, which is precisely controlled by a computer program. The time-dependent influence of the pump pulse on the polarization state of the reflected or transmitted probe pulse may then be measured. The measured time-dependent rotation can be generally related to the transient magnetic state of material, including

Table 2.1: Independent nonvanishing elements of $\chi^{(2)}(\mathbf{M})$ for the (001) surface of fcc crystals with surface magnetization $\mathbf{M}$ along the [100], [110], and [001] directions. (x is parallel to the [001] direction and the surface is in the x-y plane.)

	Independent nonvanishing elements	
Direction of $\mathbf{M}$	Even parity	Odd parity
[100]	xzx=xyz, yzy=yyz, zxx, zyy, zzz	xyx=xxy, yxx, yyy, yzz, zyz=zzy
[110]	xyz=xzy=yzx=yxz, xzx=xxz=yzy=yyz, zxx=zyy, zzz, zxy=zyx	xxx=-yyy, xyy=-yxxx, xzz=-yzz, xxy=xyx=-yxy=-yyx, zxz=zzx=-zyz=-zzy
[001]	xzx=xxz=yzy=yyz, zxx=zyy, zzz	xyz=xzy=yzx=yxz, zxy=zyx

magnetization $\mathbf{M}$(t) or coherent spins $\mathbf{S}$(t), in a phenomenological way by [48]

$$\Theta_K(t) = f[\mathbf{M}(t), t] = a(t) + \sum_{i=x}^{z} b_i(t) M_i(t), \tag{2.7}$$

where f is a function of $\mathbf{M}$ and t, and the complex quantities $a(t)$ and $b_i(t)$ are effective Fresnel coefficients depending on the refractive index, the magneto-optical coupling constant, and the optical anisotropy independent of the magnetization. If $a(t)$ and $b_i(t)$ are time independent, one can easily derive the following relationship: $\Delta\Theta_K(t)/\Theta_K(t) = \Delta M(t)/M(t)$ or $\Delta\theta(t)/\theta(t) = \Delta\varepsilon(t)/\varepsilon(t) = \Delta M(t)/M(t)$, which shows that the change in Kerr rotation or Kerr ellipticity is directly proportional to the change in magnetization. In this case, the magneto-optical signal is a complete reflection of the spin dynamics. However, $a(t)$ and $b_i(t)$ are very likely to be time-dependent, generally speaking, $\Delta M(t)/M(t) \neq \Delta\Theta_K(t)/\Theta_K(t)$. Therefore, the induced magneto-optical signal may not always reflect genuine magnetization (spin) dynamics [35]. Comparing the transient Kerr rotation and ellipticity response simultaneously will be greatly helpful in unraveling the results derived from

Table 2.2: Independent nonvanishing elements of $\chi^{(2)}(\mathbf{M})$ for the (001) surface of fcc crystals with surface magnetization $\mathbf{M}$ along the [001] and [110] directions. (x is parallel to the [001] direction and the surface is in the x-y plane.)

	Independent nonvanishing elements	
Direction of $\mathbf{M}$	Even parity	Odd parity
[001]	xzx=xxz, yzy=yyz, zxx, zyy, zzz	xxx, xyy, xzz, yxy=yyx, zxz=zzx
[110]	xzx=xxz, yzy=yyz, zxx, zyy, zzz	xyz=xzy, yzx=yxz, zxy=zyx

ultrafast magneto-optical experiments. Indeed, several experimental efforts involving femtosecond demagnetization have been carried out recently, and have provided some important insights. For example, Koopmans et al. [18] compared simultaneously the detected Kerr rotation and Kerr ellipticity using the time-resolved MOKE technique on Ni films, and found that the magneto-optical response from the magnetization dynamics dominates after 500 fs or so, while signals below 0.5 ps are due to so-called "dichroic bleaching". While, in the similar time-resolved measurements on $CoPt_3$ performed by Bigot et al. [49], the results demonstrate that spin dynamics dominates the magneto-optic signal immediately after the thermalization time of the electrons ($\sim$50 fs), and no "dichroic bleaching" effect occurs. So it is clear that the details of the ultrafast time-resolved magneto-optic signal (below the initial $\sim$1 ps) is strongly materials dependent.

2.5 Optical Setup

A schematic of our experimental setup used for time-resolved magneto-optics measurements is shown in Figure 2.3. One can see that the configuration shown in Figure 2.3 is a typical one-color pump-probe setup, wherein a pulsed Ti:Sapphire (Coherent Mira) laser system is employed. This laser system has a pulse width about 150

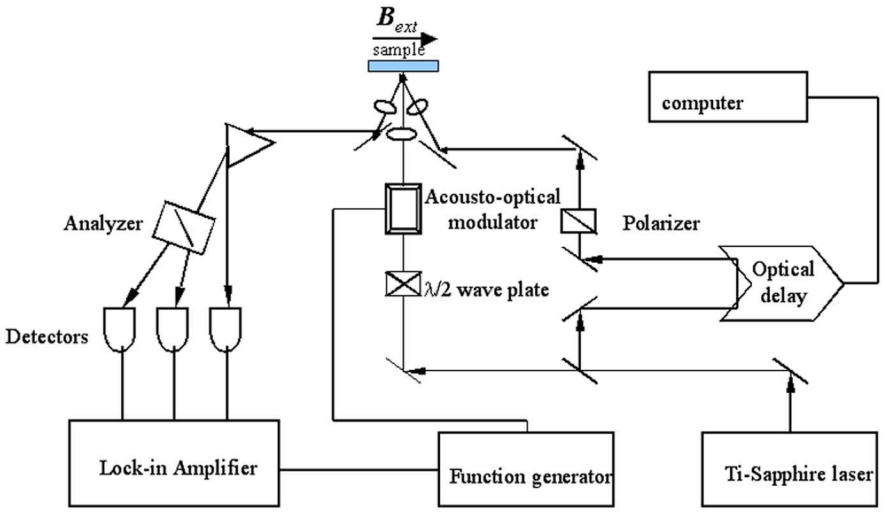

Figure 2.3: Schematic representation of the experimental setup for TRMOKE and time-resolved SHG.

fs, a repetition rate of 76 MHz, and a wavelength range from 710 nm to 950 nm. The intensity of pump light is modulated using an acousto-optic modulator with a frequency (52 kHz), which is used as the reference frequency as input to the lock-in amplifier. A quarter-wave plate or photoelastic modulator is also placed in the path of the pump light to modifiy the polarization of the light to be either linear or circular (left or right). The pump pulse is focused onto the sample by a lens in front of the cryostat with a spot diameter from 60 μm to 100 μm. The probe pulse is adjusted by a computer-controlled translation stage (Newport). Thus, the magneto-optical response experienced by the delayed probe pulses can be measured as a function of time delay between pump and probe pulses. The probe pulse is usually linearly polarized, and is focused onto the sample within the confines of the pump spot. The temperature of the sample in the cryostat can be changed from liquid helium temperature ($\sim$4 K) to room temperature. An external magnetic field up to 300 mT can be added with its direction perpendicular to the plane determined by the incident and the reflected beams. In this class of experiments, where small transient variations of the polarization are of interest, fast fluctuations of the sample reflectivity due to the excitation and relaxation of carriers are a common concern. In our experiments, the

influences of these contributions were minimized by using a very sensitive balanced detection scheme [35](see also Appendix B). In this scheme, a Wollaston prism is used to split the reflected probe beam into two spatially separated components with polarization directions orthogonal to each other. The corresponding intensities are detected with a pair of equivalent photodiodes and then subtracted through a differential amplification circuit. The output signal, proportional to the Kerr rotation θ (or to the Kerr ellipticity ε measured with a quarter-wave plate in front of the prism) is then measured at 52 kHz with a lock-in amplifier. This sensitive balanced detection technique allows for the measurement of very tiny pump-induced polarization changes in the sample down to the order of microrad. If the time-resolved second harmonic generation signal is to be measured, a triangular prism is employed to spatially separate the reflected beams with fundamental frequency ω and doubled frequency 2ω, respectively. The second harmonic beam is then introduced into a photon-multiplied tube after passing through the analyzer and the filter. Figure 2.4 is a schematic representation of a static nonlinear magneto-optical measurement (MSHG) setup. For this class of experiments, no pump pulse is required and the sample is kept at room temperature. Here, measurements may be made as a function of external magnetic field which may range from 0 to 500 mT and as a function of the polarization of the incident and reflected light beams. The magnetic field may be applied either along the longitudinal direction or along the transverse direction. The detection part is very similar with that in Figure 2.3.

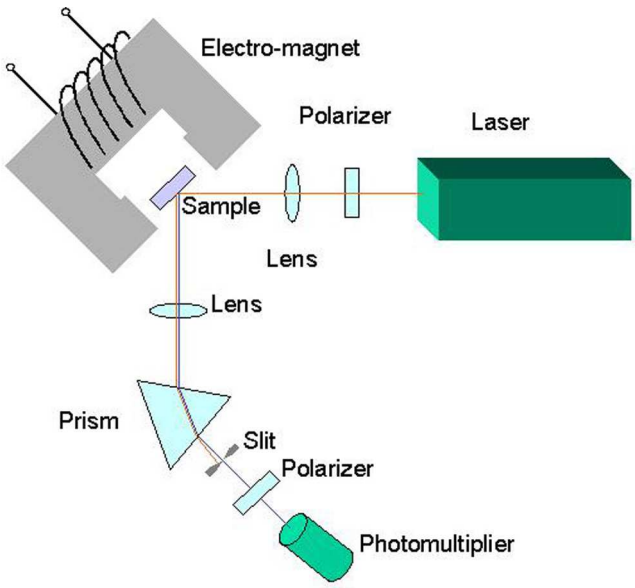

Figure 2.4: Schematic representation of the experimental setup for MSHG experiments.

CHAPTER III

(III,Mn)V DILUTED MAGNETIC SEMICONDUCTORS

3.1 Introduction

Semiconductor based integrated circuits, which rely solely on the manipulation of the charge of electrons in semiconductors, have had a singularly revolutionary impact on our society. More recently, mass data storage has been greatly facilitated by the use of magnetic recording devices employing the spin of the electron in ferromagnetic metals. However, the ferromagnetic material structures used in magnetic recording are not easily incorporated into nor are they compatible with typical semiconductor device structures [50]. Therefore, in recent years much research has been devoted to the realization of material structures which combine semiconducting properties with robust magnetism [28, 50, 51, 52, 53, 54].

In order to make use of both the charge and the spin of electrons in semiconductors, researchers have incorporated a relatively high concentration of magnetic ions into currently widely-used nonmagnetic III-V semiconductors. Doping with the magnetic impurities can lead to p- or n-type magnetic semiconductors, which constitute a new class of materials known as diluted magnetic semiconductors(DMSs) [28]. The introduction of III-V DMSs opens up new and exciting opportunities to make use of magnetic phenomena in conventional electrical and optical devices. Among all DMS systems, (Ga,Mn)As is one of the most extensively studied system, both experimentally and theoretically [27, 28, 50, 55]. The principal focus of this dissertation is on studies of (Ga,Mn)As ferromagnetic semiconductor structures.

3.2 Basics of III-V Semiconductors

3.2.1 Band structure of intrinsic III-V semiconductors

The host materials for (III,Mn)V DMSs are III-V semiconductors. Clearly, a comprehensive understanding of the physical properties of these III-V semiconductors

is essential. In particular, elucidating the electronic structure of semiconductors is fundamental to the understanding of many relevant physical phenomena [56]. III-V and II-VI materials are direct band-gap semiconductors with an inversion-asymmetric zinc-blende structure. These materials have a very similar band structure with the smallest band gap between valence band and conduction band at the Γ point $\boldsymbol{k}$=0. Detailed calculations of the band structure of these semiconductors can be carried out using a variety of different theoretical models, among which the $\boldsymbol{k}\cdot\boldsymbol{p}$ method with the envelope function approximation can obtain the band structures in the vicinity of any $\boldsymbol{k} = \boldsymbol{k}_0$ point in the k-space [57, 58]. The derivation of the $\boldsymbol{k}\cdot\boldsymbol{p}$ method is based on the Schrödinger equation, where the wave-functions are Bloch like, arising from the microscopic lattice-periodic crystal potential. After some general symmetry considerations in terms of the crystal lattice, appropriate basis functions can be chosen to make up the wave-functions and decompose the Hamiltonian to simply the calculations.

The zinc-blende crystal is characterized by point group T_d. In the language of group theory, point group T_d at the zone center Γ is decomposed into several irreducible representations: two one-dimensional (Γ_1 and Γ_2), one two-dimensional (Γ_3), and two three-dimensional (Γ_4 and Γ_5) [59, 60]. Under the tight-binding picture, sp_3 hybridization consists of the topmost bonding p-like (X, Y, Z) valence band states and the antibonding s-like (S) and p-like (X, Y, Z) lowest conduction band states. The s-like state (l=0) transforms according to the irreducible representation Γ_1, and the p-like states (l=1) transform according to the irreducible representation Γ_5(valence band Γ_1^v and conduction band Γ_1^c). In the calculation of the exact band structure, spin-orbit (SO) coupling should be taken into account. With this consideration, the band states transform according to the irreducible representations from the double group $T_d \otimes D_{1/2}$ [59, 60], which breaks up into two one-dimensional (Γ_1 and Γ_2), three two-dimensional (Γ_3, Γ_6 and Γ_7), two three-dimensional (Γ_4 and Γ_5), and one four-dimensional (Γ_8). Now the lowest conduction band transforms according to Γ_6^c. The

previous topmost Γ_5^v valence bands split into four-fold degenerate states |j=3/2,m> and two-fold degenerate states |j=1/2,m>. |j=3/2,m> and |j=1/2,m> transform according to Γ_8^v and Γ_7^v, respectively. Now the Γ_8^v bands are the topmost valence bands, and Γ_7^v bands are often called the "spin split-off bands" [56]. The energy splitting between Γ_6^c and Γ_8^v is the usually called "the energy band gap E_g". Here j is the total angular momentum given by $l \pm s$, where $l(= 0, 1, 2...)$ and s(=1/2) are the orbit and spin momentum, respectively. m (|m|≤j) is the momentum quantum number. Detailed basis functions for the above irreducible representations in terms of the orbital states and spin states are given in Table 3.1 [58]. The energy bands in the vicinity of Γ point are schematically shown on figure 3.1.

Table 3.1: Some basis functions of the double group ($T_d \otimes D_{1/2}$) in the vicinity of Γ point in a zinc-blende crystal.

Γ_8^c	$\|3/2,3/2\rangle_c = \frac{-1}{\sqrt{2}}\|\begin{smallmatrix}X+iY\\0\end{smallmatrix}\rangle$	$\|3/2,1/2\rangle_c = \frac{1}{\sqrt{6}}\|\begin{smallmatrix}2Z\\-X-iY\end{smallmatrix}\rangle$
	$\|3/2,-1/2\rangle_c = \frac{1}{\sqrt{6}}\|\begin{smallmatrix}X-iY\\2Z\end{smallmatrix}\rangle$	$\|3/2,-3/2\rangle_c = \frac{-1}{\sqrt{2}}\|\begin{smallmatrix}0\\X-iY\end{smallmatrix}\rangle$
Γ_7^c	$\|1/2,1/2\rangle_c = \frac{-1}{\sqrt{3}}\|\begin{smallmatrix}Z\\X+iY\end{smallmatrix}\rangle$	$\|1/2,-1/2\rangle_c = \frac{-1}{\sqrt{3}}\|\begin{smallmatrix}X-iY\\-Z\end{smallmatrix}\rangle$
Γ_6^c	$\|1/2,1/2\rangle_c = \|\begin{smallmatrix}S\\0\end{smallmatrix}\rangle$	$\|1/2,-1/2\rangle_c = \|\begin{smallmatrix}0\\S\end{smallmatrix}\rangle$
Γ_8^v	$\|3/2,3/2\rangle_v = \frac{-1}{\sqrt{2}}\|\begin{smallmatrix}X+iY\\0\end{smallmatrix}\rangle$	$\|3/2,1/2\rangle_v = \frac{1}{\sqrt{6}}\|\begin{smallmatrix}2Z\\-X-iY\end{smallmatrix}\rangle$
	$\|3/2,-1/2\rangle_v = \frac{1}{\sqrt{6}}\|\begin{smallmatrix}X-iY\\2Z\end{smallmatrix}\rangle$	$\|3/2,-3/2\rangle_v = \frac{-1}{\sqrt{2}}\|\begin{smallmatrix}0\\X-iY\end{smallmatrix}\rangle$
Γ_7^v	$\|1/2,1/2\rangle_v = \frac{-1}{\sqrt{3}}\|\begin{smallmatrix}Z\\X+iY\end{smallmatrix}\rangle$	$\|1/2,-1/2\rangle_v = \frac{-1}{\sqrt{3}}\|\begin{smallmatrix}X-iY\\-Z\end{smallmatrix}\rangle$

3.2.2 Optical selection rules

To obtain excitation (or de-excitation) probabilities, one needs to calculate the transition matrix from the initial state $|\Psi_i>$ to the final state $|\Psi_f>$, which is given by $\langle\Psi_f|e\vec{r}\cdot\vec{E}|\Psi_i\rangle$. The probability is proportional to $|\langle\Psi_f|e\vec{r}\cdot\vec{E}|\Psi_i\rangle|^2$. Choosing the quantization axis of angular momentum along the crystallographic direction [001], which is parallel to the propagation direction of the photons, we can write down the

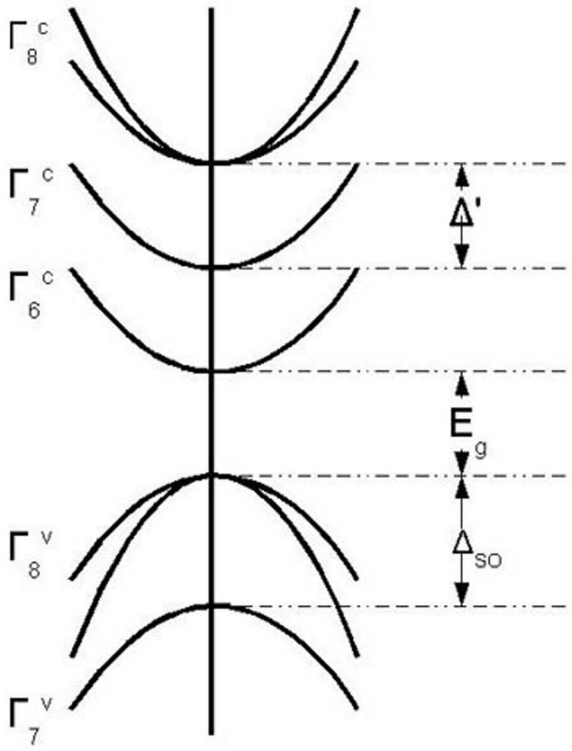

Figure 3.1: Schematic band structure around the Γ point.

polarization vectors for $\sigma+$ and σ- helicity as

$$\vec{r}_R = -\frac{(X+iY)}{\sqrt{2}} \qquad \vec{r}_L = \frac{(X-iY)}{\sqrt{2}}, \tag{3.1}$$

where (X±iY) is proportional to $Y_1^{\pm 1}$, where Y_l^m is a spherical harmonic function [5]. By considering the transition probability governing the excitation from a valence band to a conduction band or vice versa, we can obtain the optical selection rules and relate them to changes in angular momentum. For instance, given a transition between an initial state |3/2,-3/2> and a final state |1/2,-1/2>, exciting with $\sigma+$ polarized light implies that the incident photon supplies angular momentum +1 to the orbital part of electronic states. This means the matrix element $eE\langle 1/2,-1/2|\vec{r}\cdot\vec{r_R}|3/2,-3/2\rangle \propto \langle 1/2,-1/2|Y_1^1|3/2,-3/2\rangle$ is not equal to zero, and consequently the transition is allowed. With the information provided in Table 3.1, the relative strength comparing a transition between a top valence heavy hole band (|m|=3/2)

and a bottom conduction band, and a transition between a light hole band (|m|=1/2) and a bottom conduction band may be evaluated as shown below.

e.g.,

$$\frac{|\langle 1/2,-1/2|Y_1^1|3/2,-3/2\rangle|^2}{|\langle 1/2,1/2|Y_1^1|3/2,-1/2\rangle|^2} = 3. \tag{3.2}$$

A schematic representation of the relative transition intensities are given in figure 3.2.

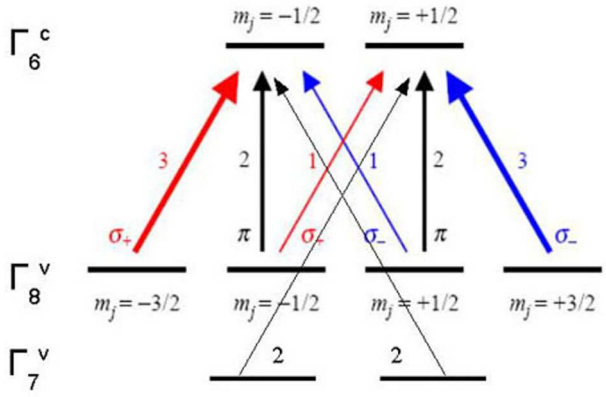

Figure 3.2: A schematic representation of the band structure around the Γ point. The arrows represent interband transitions in GaAs between m_j sublevels for circularly polarized light σ, and linear polarized light π. The numbers denote the relative transition intensities for all excitations (depicted by the arrows) and de-excitations.

3.2.3 III-V semiconductors doped with nonmagnetic impurities

From the previous section, intrinsic (undoped) III-V semiconductors are characterized by a direct energy band gap. Upon excitation by external means (e.g., thermally, optically etc.), the concentration of electrons in conduction band and holes in valence band are equal: $n_e = n_h exp(-E_g/2k_BT)$ [61]. When certain impurities are introduced, the carrier concentration can be manipulated. These impurity atoms are classified into donors and acceptors, which result in either n- or p-type semiconductors, respectively [56, 61]. One example is that Si may replace Ga in GaAs. Si has one more valence electron and acts as donor. If Ga is replaced by Zn in GaAs, impurity Zn acts as

acceptor because Zn has one less valence electron and introduces an extra hole. In these examples, the electron (hole) is weakly bound to the Si^{4+} (Zn^{2+}), and forms a hydrogenic shallow donor (acceptor) state. Thus the excitation energy required to make the semiconductor into a conductor is markedly reduced (see figure 3.3).

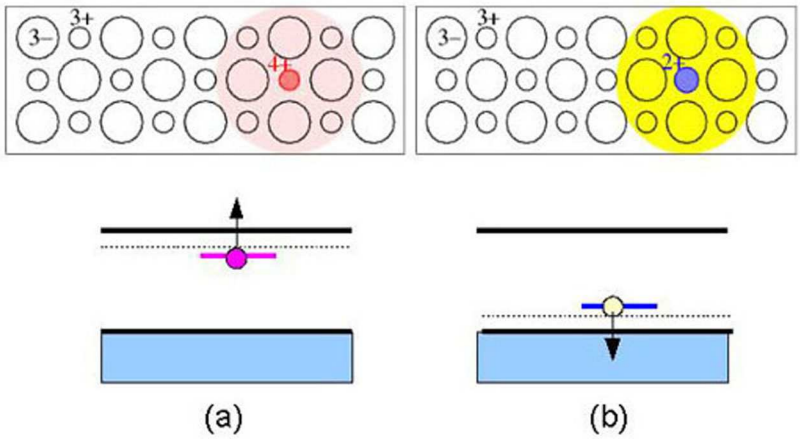

Figure 3.3: Visualization of (a) donor and (b) acceptor, and their energy band diagram representations, respectively.

If impurity in the crystal field has levels close to mid-gap, deep levels rise up and are not hydrogenic any more. e.g., Te in GaAs [62]. However, both shallow and deep levels can also result from native defects such as vacancies, interstitials and so on. They may lower carrier concentration (or compensation) if donors and acceptors are present. Continuously increasing the doping level further might result in hydrogenic impurity states forming impurity band and even overlap with the valence band or conduction band [28, 63](see figure 3.4).

3.3 Ferromagnetic Semiconductor (Ga,Mn)As

3.3.1 Physical properties of ferromagnetic (Ga,Mn)As

When grown under equilibrium conditions, the Mn doping level x cannot exceed 0.1% in the $Ga_{1-x}Mn_xAs$ [28]. The Mn in these materials can be expected to be exclusively occupying the the low-energy Ga-Substitutional site. Ferromagnetism, however, is

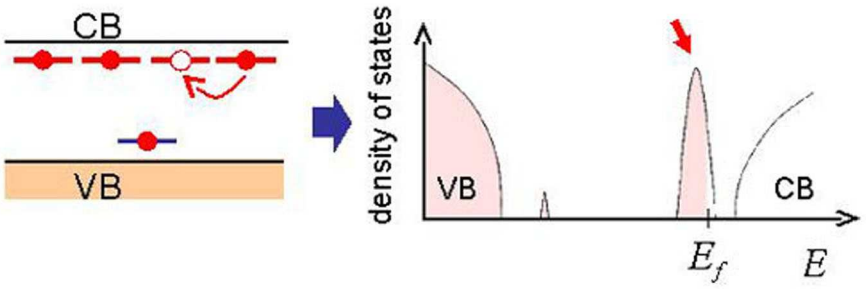

Figure 3.4: Schematic pictures of impurity bands.

only observed for (Ga,Mn)As when Mn concentration is larger than about 1%, which is well above the equilibrium solubility causing Mn precipitation to appear (or in some instances a MnAs alloy), which can be avoided in practice by low temperature grown molecular beam epitaxy(LT-MBE) [50]. To date, the largest ferromagnetic transition temperature in (Ga,Mn)As occurs for x$\sim$8%, the record Curie temperature T_C being about $\sim$150 K [64], still below room temperature.

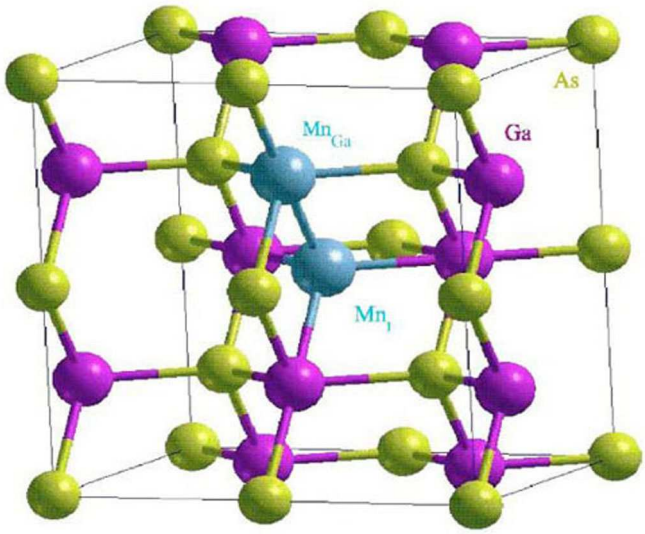

Figure 3.5: Visualization of substitutional Mn_{Ga} and interstitial Mn_I.

The elements in the (Ga,Mn)As compound have nominal atomic structures of [Ar]$3d^{10}4s^2p^1$ for Ga, [Ar]$3d^5 4s^2$ for Mn, and [Ar]$3d^{10}4s^2p^3$ for As. The most com-

mon and stable position for Mn in the GaAs host lattice is on the Ga site. Positions are illustrated in figure 3.5. The missing 4p electron causes the substitutional Mn_{Ga} impurity to act as an acceptor, whose charge is Mn^{2+}. Electron paramagnetic resonance and optical experiments [28] demonstrate that Mn_{Ga} has a local angular momentum S=5/2 and an orbital moment L=0. The price paid for LT-MBE growth is the occurrence of a large number of metastable impurities. The most important additional defects are interstitial Mn ions and As antisites (As atoms on cation sites) [28]. Mn composition x in $Ga_{1-x}Mn_xAs$ films is determined by X-ray diffraction measurements (XRD). The lattice constant a of (Ga,Mn)As follows Vegard's law, and can be described as

$$a = a_0 + a_s x_s \qquad \text{nm}, \tag{3.3}$$

where a_0 is the GaAs lattice constant, a_s is the expansion coefficient ranging from -0.05 to 0.02, and x_s is the Mn_{Ga} density. Generally, x does not equal x_s, so the relationship between a and x contains some error because the lattice constant is dependent on the growth conditions such as the substrate temperature and As overpressure (i.e., interstitial Mn ions and As antisite incorporation). According to the more reliable calculations and experimental available data, the composition-dependent lattice constant is found to obey [65]

$$a(x_s, x_i, y) = a_0 - 0.05x_s + 0.48x_i + 0.46y \qquad \text{nm}, \tag{3.4}$$

where x_i and y are the concentrations of Mn_I and As_{Ga}, respectively.

From Eqs. (3.3) and (3.4), as expected, the lattice constant a changes only weakly with the Mn_{Ga} concentration x_s, and is dominated by Mn_I and As_{Ga}(see also figure 3.6) defects. Recent experiments confirmed that both defects result in a significant expansion of the lattice[65, 66].

The presence of ferromagnetism can be revealed by magnetization measurements using a superconducting quantum interference device (SQUID)[50]. As shown in figure 3.7[50], sharp and square hysteresis loops, indicating a well-ordered ferromagnetic

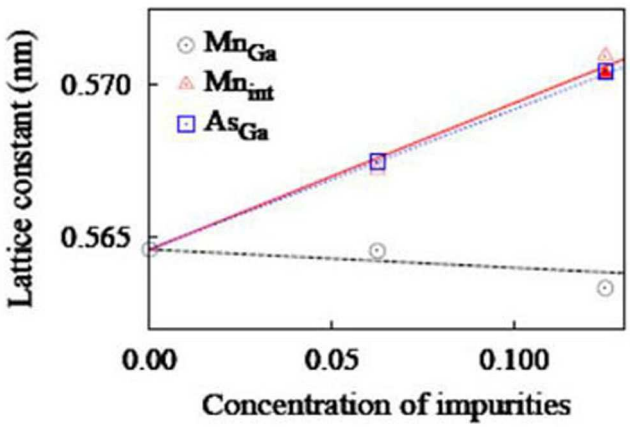

Figure 3.6: Theoretical lattice constant of GaMnAs as a function of Mn_{Ga}, Mn_I, and As_{Ga}, respectively.

structure, appeared in the magnetization (M) versus magnetic field (B) curves when B was applied in the plane of the (Ga,Mn)As films. By recording the magnetization versus various temperatures, one can obtain the Curie temperature for a given magnetic semiconductor.

All the previous experimental measurements and theoretical calculations show that the Curie temperature for (Ga,Mn)As increases with the free hole concentration increasing, which can be realized in practice by post-annealing procedures [64]. This fact is also observed in the measurement of conductivity (or resistivity). Magneto-transport studies, including the temperature-dependent conductivity (resistivity) and Hall effects, can provide much more information about the DMS materials [28]. The studies demonstrate that (Ga,Mn)As materials can exhibit insulating or metallic behavior depending on growth parameters of MBE (see figure 3.8)[50]. The sheet Hall resistivity R_{Hall} (or the Hall resistivity ρ_{Hall}) in magnetic materials is given by

$$R_{Hall} = \frac{R_O B + R_A M}{d} \qquad (\rho_{Hall} = R_O B + R_A M), \tag{3.5}$$

where R_O is the ordinary Hall coefficient, R_A the anomalous Hall coefficient, d the sample thickness, and M the magnetization of the sample.

An important finding from the Hall effect experiments is shown in figure 3.9[50].

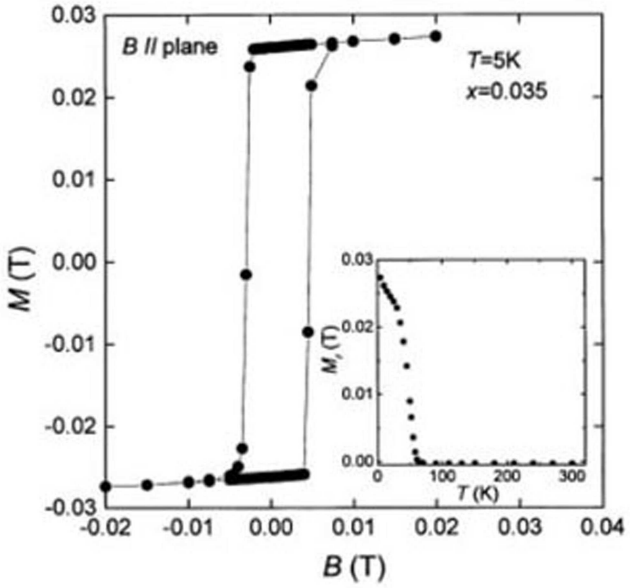

Figure 3.7: Magnetic hysteresis loop for GaMnAs with Mn content 0.035 at 5 K. The magnetic field was applied along the sample surface. The inset shows the temperature dependence of the remanent magnetization of the same sample.

It can be seen from Fig. 3.9 that the (Ga,Mn)As experiences the metal-insulator transition upon changes in the Mn doping level. Samples with an intermediate Mn composition (x from 0.035 to 0.053) are around the transition edge. Near the Curie temperature, the temperature-dependent resistivity exhibits a shoulder in all the curves, especially pronounced in the more metallic samples. This anomalous behavior is most probably due to critical scattering, where carriers are scattered by magnetic fluctuations through exchange interactions [67].

In addition to the magnetization, some other parameters are often employed to phenomenologically describe the long range properties of ferromagnets. One critical parameter is the magnetic anisotropy [28], which usually depends on the symmetry of the system. The magnetic anisotropy of (Ga,Mn)As ferromagnets is a combination of the cubic magneto-crystalline term, the in-plane uniaxial anisotropy, and the uniaxial term induced by the growth-direction lattice-matching strain which often dominates in (Ga,Mn)As epilayers [28]. The magneto-crystalline anisotropy depends on the mag-

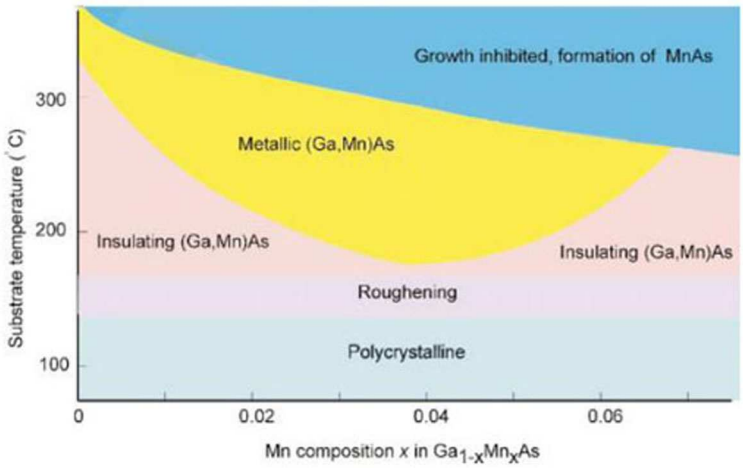

Figure 3.8: Schematic phase diagram showing the relationship between GaMnAs properties and growth parameters (substrate temperature and Mn concentration).

netization orientation with respect to the crystallographic axes, and is a spin-orbit coupling effect often associated with localized electrons in magnetic d or f shells. In (Ga,Mn)As, the physical origin of the magneto-crystalline anisotropy is spin-orbit coupling in the valence band [68]. In the LT-MBE growth of the (Ga,Mn)As, it is inevitable (mentioned above) that interstitial Mn_I and As_{Ga} antisites will be incorporated into the DMS crystal, and result in relaxed (Ga,Mn)As lattice constants of larger than that of GaAs. Therefore, (Ga,Mn)As grown on a GaAs substrate is under compressive strain. Strain in the [001] growth direction breaks the cubic symmetry of (Ga,Mn)As, leading to the magnetic anisotropy energy as functions of cubic and uniaxial anisotropy [68]. In particular, theory and experiment show that the easy axis is in plane for compressive strain, and out of plane for tensile strain [28, 69].

3.3.2 Origin of Ferromagnetism in (III,Mn)V Semiconductors

For (Ga,Mn)As and some other (III,Mn)V ferromagnets the local Mn moments are the origin of the magnetism [28]. However, the phenomena of magnetic order require

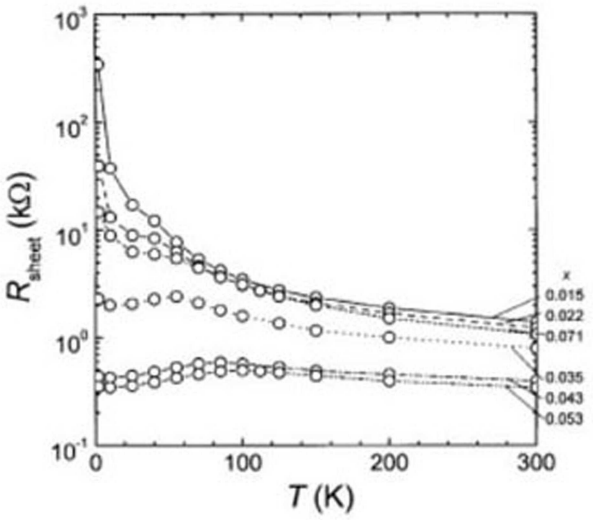

Figure 3.9: Temperature dependence of the sheet resistivity of GaMnAs thin films. The range of the Mn concentration is from 0.015 to 0.071. Samples with intermediate composition (0.035-0.053) are metallic.

interaction between magnetic moments, implying that the energy of the system depends on the relative orientation of Mn moments. The first interaction that might be expected to play a role is the magnetic dipole-dipole interaction. The order of magnitude of this effect can be estimated to be approximately 1 K with a separation of $\sim$1 angstrom (a lattice constant). Such a small value is too weak to account for the magnetic ordering in many condensed matter systems [70]. Another interaction, lying at the heart of the phenomenon of long range magnetic order, is generally called the exchange interaction, and is ultimately derived from the fermionic quantum statistics of electrons [70]. A spin-dependent term in the effective Hamiltonian for a two-electron system can be simply obtained $H^{spin} = -2J\mathbf{S}_1 \cdot \mathbf{S}_2$ [70], where J is defined as exchange constant (or exchange integral). When generalizing to many-body system, a similar spin-dependent term as that in the two-electron system may be applied, and thus motivates the Hamiltonian of the Heisenberg model: $H = -2J_{ij}\mathbf{S}_i \cdot \mathbf{S}_j$, where J_{ij} is the exchange constant between the ith and jth spins. There are several types of magnetic exchange interactions that can be separately identified when address-

ing the magnetic order in (III,Mn)V magnetic semiconductors. However, the doping regime and the host material will influence the relative importance of different effects and their applications [28]. Direct exchange, where the electrons on localized neighboring magnetic atoms interact via an exchange interaction, proceeds directly without the need for an intermediary. The direct exchange itself may not be a dominant mechanism in controlling the magnetic properties in most cases because of the insufficient direct overlapping between neighboring magnetic orbitals in most cases, making it necessary to consider some kind of indirect exchange (or kinetic exchange) interactions [28, 70]. An indirect exchange interaction, known as superexchange, acts between non-neighboring magnetic ions, which is mediated by a non-magnetic ion sitting among the magnetic ions. In a crystal environment, an electron of a non-magnetic ion can be transferred to the empty shell of a magnetic ion and interact, via direct exchange, with electrons forming its local moments. On the other hand, the non-magnetic ion is polarized and coupled via direct exchange with all its other neighboring magnetic ions. Whether the superexchange interaction leads to ferromagnetic or antiferromagnetic coupling is determined by the relative signs and strengths of the different direct coupling constants [70]. An example can be seen in figure 3.10. In (Ga,Mn)As system, superexchange gives an antiferromagnetic contribution to the interaction between Mn moments located on neighboring cation sites.

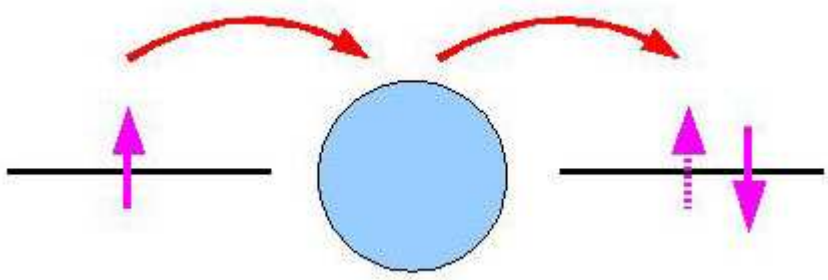

Figure 3.10: Schematic diagram for the superexchange through intervening nonmagnetic ions. e.g. FeO and MnO.

In some magnetic materials, a ferromagnetic exchange interaction occurs because the magnetic ion can show mixed valency (or partially filled shells). The ferromagnetic alignment is due to the double exchange mechanism, which can be understood with reference to figure 3.11 [70]. The e_g electron on a Mn^{3+} ion can hop to a neighboring site only if there is a vacancy there of the same spin. The hopping proceeds without spin-flip of the hopping electron. This presents no problem since the Mn^{4+} has no electrons in its e_g shell. According to Hund's first rule, the exchange interaction between e_g electron and the other three t_{2g} electrons will lead to align them in the same direction. Thus ferromagnetic alignment of neighboring ions is required to maintain the high-spin arrangement on both the donating and receiving ion. Because the hopping process saves the overall energy, the system prefers being ferromagnetically aligned. Moreover, the ferromagnetic alignment then allows the e_g electrons to hop through the crystal and the materials becomes metallic. A version of double exchange, being often referred to in the (III,Mn)V literature, is that the Mn acceptor states form an impurity band with mixed *spd* character. In this picture, both electric conduction and Mn-Mn exchange coupling are realized via hopping with an impurity band. The potential importance of double exchange is greater at lower Mn doping and in wider-gap (III,Mn)V magnetic semiconductors [28].

Another important indirect exchange interaction is the so-called Zener kinetic exchange interaction [71]. In many cases, the coupling between magnetic moments is mediated by the s- or p-band itinerant carriers. A local magnetic moment can undergo ferromagnetic direct exchange coupling with the carriers on the same or neighboring site. The polarized carriers in turn couple to another neighboring localized magnetic moment. When this coupling is weak, it is often described by the RKKY theory [70]. Depending on the separation between the neighboring magnetic moments, the coupling can be either ferromagnetic or antiferromagnetic and tends to vary in space on the length scale of the itinerant band's Fermi wavelength. Obviously, this kind of exchange interaction does play an important role in (III,Mn)V ferromagnetism [28].

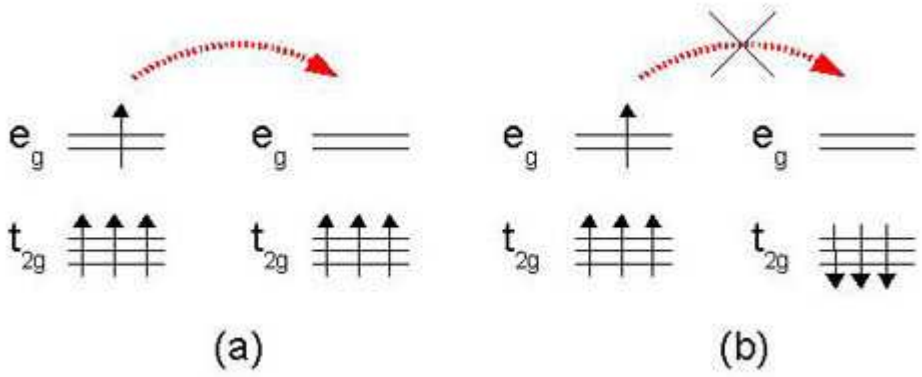

Figure 3.11: Double exchange mechanism leads to ferromagnetic coupling between Mn^{3+} and Mn^{4+} ions participating in electron transfer. The single-center exchange interaction favors hopping if (a) neighboring ions are ferromagnetically aligned and not if (b) neighboring ions are antiferromagnetically aligned.

3.3.3 Electronic Structure of Ferromagnetic (Ga,Mn)As

When theoretically explaining the carrier mediated ferromagnetism in (Ga,Mn)As, it is fundamentally important to identify the band where itinerant carriers reside [72, 73]. In the low Mn concentration regime ($x <\sim 0.04$), it is generally believed that the holes from the Mn-induced impurity band (IB), which interact with the substitutional Mn_{Ga}, contribute to the ferromagnetism [74]. This picture is consistent with the fact that Mn_{Ga} forms a shallow acceptor level in the host GaAs when the doping is weak ($\sim 10^{17} cm^{-3}$) [75]. However, the nature of states in the heavily doped (Ga,Mn)As with high ferromagnetic transition temperature (T_C) remains controversial [72, 73]. In addition to the IB picture, one scenario states that in the high doping regime the holes are doped into the GaAs valence band (VB) from the Mn acceptor levels. This scenario is based on the assumption that $Ga_{1-x}Mn_xAs$ falls within the Mott picture of the metal-insulator transition (MIT), wherein the IB finally dissolves into the GaAs VB [55]. Another alternative scenario is the so-called disordered valence-band picture where the IB and the host VB merge into one inseparable band [73]. Three different pictures are illustrated in Fig. 3.12.

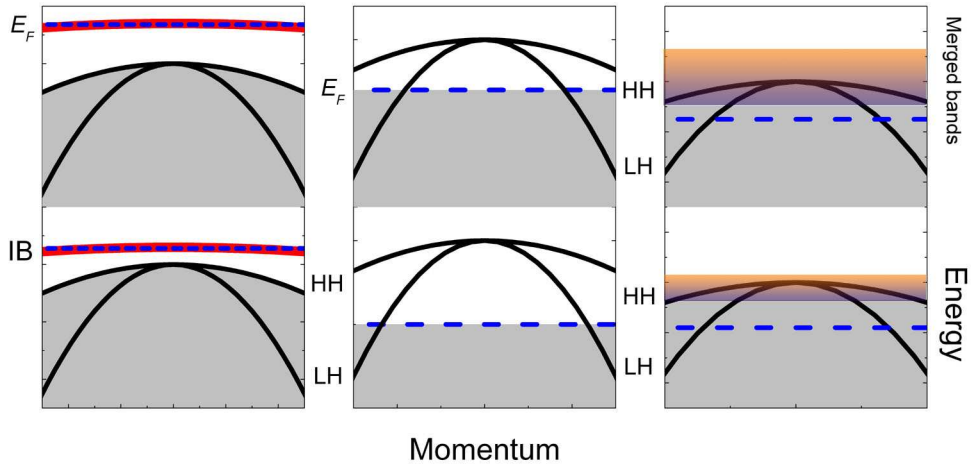

Figure 3.12: Three scenarios for the electronic structure of GaMnAs. From left to right, (a) E_F lies in the IB which is above the top of VB; (b) E_F sits inside the VB; (c) E_F is inside the disordered VB, where the IB and VB merge. The top and bottom are the low and high doping regimes, respectively.

3.4 Prior Experiments on Ultrafast Dynamics of (Ga,Mn)As

Of all the experimental techniques, the time-resolved magneto-optical Kerr effect (TRMOKE) is a good method to study the ultrafast photoinduced magnetization dynamics, and has already been performed in (Ga,Mn)As by several groups. One of the pioneering works was done by Kojima et al. [76], who carried out a two-color TRMOKE measurement on a ferromagnetic semiconductor $Ga_{0.95}Mn_{0.05}As$ sample with 1.05 μm thickness. In their experiment, a very slow thermalization of the spin temperature was found, even much slower than that of the hole and the lattice systems (see figure 3.13). They concluded that the spin-thermal isolation exists in this system, which behaves with a half-metallic feature.

Later, Kimel et al. [77] reported their observation of TRMOKE on the (Ga,Mn)As system. They found that the magnetization (or spin) dynamics are only related to the coherent electron spins in the conduction band with an almost constant decay time (see figure 3.14). Their observation demonstrates a weak interaction (or weak

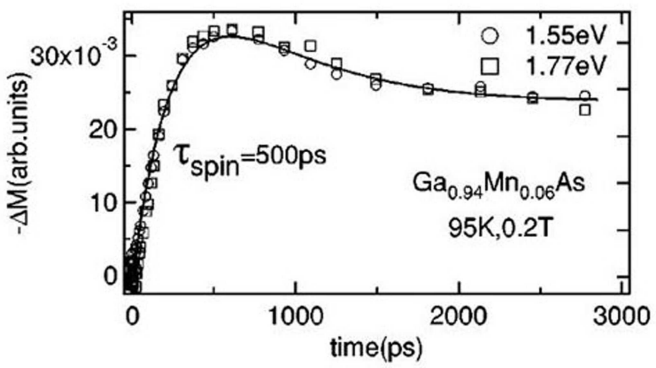

Figure 3.13: Temporal evolution of the magnetization component. The open circles are from Kerr rotation and Kerr ellipticity at 1.55 eV, and the open squares are from Kerr rotation and Kerr ellipticity at 1.77 eV. The open circles and squares are normalized at the maximum point. The solid line represents simulated results using a three temperature model.

coupling) between the spins of electrons in the conduction band and spins of Mn ions.

One work done on GaMnAs by Munekata's group, who optically injected spin polarized carriers, showed that the photo-induced magnetization process includes contributions from both the free carrier spins with short spin lifetime and the coupled hole-Mn complex spins with relatively long spin lifetime. This process involves a magnetization rotation from in-plane to out-of-plane and gives rise to a temporal Kerr rotation signal [78]. In two other experiments done by the same group, photo-induced magnetization precession was found in a long time domain [79, 80]. This phenomenon was explained by a change in hole concentration and the resultant change in magnetic anisotropy. Although the same conclusion was obtained, contradictory experimental results were found (see figure 3.15).

Although in (Ga,Mn)As the ferromagnetism is believed to be mediated by free carriers and highly nonthermal control of the magnetization by light was reported in static measurements [81], the photo-enhanced magnetization in dynamic measurements was only recently observed by Wang et al. (see figure 3.16) [82], and has not been reproduced by other groups.

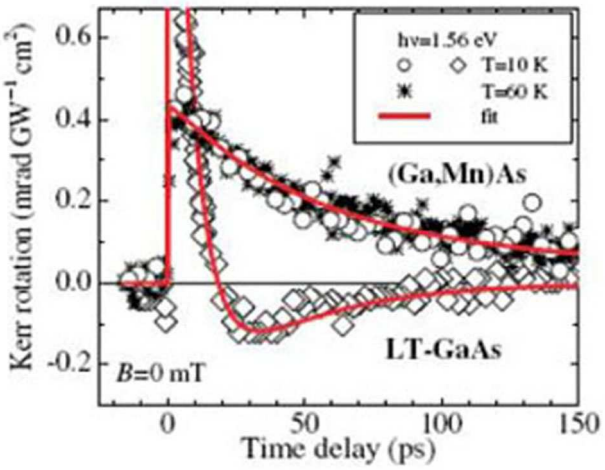

Figure 3.14: TRMOKE signal for GaMnAs at temperatures 10 K and 60 K, respectively. For comparison, the data from LT-GaAs are also shown. The photon energy is 1.56 eV. The solid lines are fitted results.

The debate about the interpretation of the magneto-optic response on (Ga,Mn)As system is mainly due to the limited and even controversial understanding of its electronic, optical, and magnetic properties [24]. Therefore, the exact description of the photo-induced magnetization dynamics in (Ga,Mn)As still needs to be clarified further.

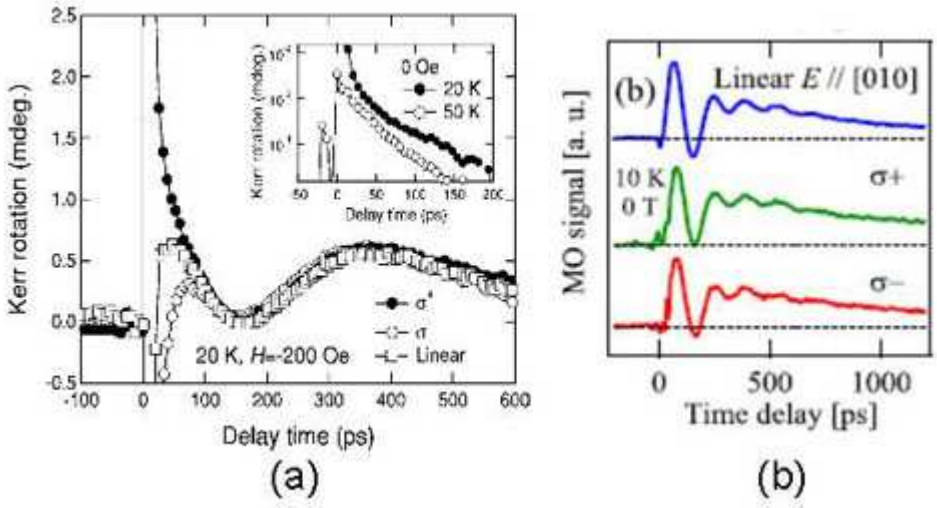

Figure 3.15: TRMOKE signals from (a) $Ga_{0.989}Mn_{0.011}As$ and (b) $Ga_{0.98}Mn_{0.02}As$ with linear, left and right circularly polarized light excitations.

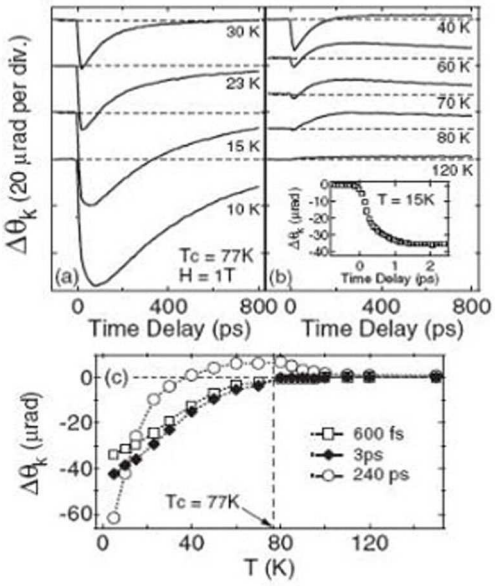

Figure 3.16: TRMOKE signals for $Ga_{0.925}Mn_{0.075}As$ at different temperatures. Temperature dependence of magnetization at different time delays.

CHAPTER IV

LIGHT-INDUCED COHERENT SPIN DYNAMICS IN FERROMAGNETIC (Ga,Mn)As SYSTEMS

4.1 Introduction

In ultrafast pump-probe magneto-optical spectroscopy experiments, the optical pump pulse may excite optical polarizations, nonthermal carrier populations, and carrier spins. This in turn will trigger coherent spin dynamic phenomena, which can be measured as a function of time [83]. To interpret the experimental results, it is important to identify and characterize the different stages of time evolution of the photoexcited system. Coherent spin phenomena can be described within the framework of several models [84, 85, 86, 87], which are useful to interpret the observed light-induced magnetization precessional motion and relaxation.

4.2 Carrier and phonon dynamics in the photo-excited semiconductors

When a semiconductor system under thermal equilibrium is excited by an ultrashort laser pulse, it undergoes several relaxation processes before it returns to thermal equilibrium [88]. These relaxation processes may be classified into several temporally overlapping regimes.

Initially, an ultrashort laser pulse may create excitation in the form of free electron-hole pairs or excitons in the semiconductor with a well-defined coherent phase relationship within the excitation and in phase with the incident electromagnetic field. This is referred to as the coherent regime.

This well-defined coherent phase relationship decays on the order of a few femtoseconds due to electron-electron, hole-hole, and electron-hole scattering processes. In the coherent regime, the distribution function of the excitation cannot be characterized by a temperature since it is far from equilibrium.

In the next time regime, because of scattering among carriers, the energy in the carrier system is redistributed and approaches a quasi-thermal distribution on a sub-

picosecond time scale. The third time regime is characterized by the creation of phonons, which mediate the exchange of energy between carriers and the lattice. In this regime, the carrier system shares its energy with the lattice through the creation of optical phonons over the time scale of a few picoseconds. Before final equilibration, the temperature characterizing the thermalized distribution function of carriers is higher than that of the lattice system. At that stage, the photoexcited system can be phenomenologically described by the so-called "two temperature model" [89]. Temperatures and specific heats are assigned separately to the carrier ($T_{e/h}$, $C_{e/h}$) and lattice (T_l,C_l) systems. It should be pointed out that the mass difference between electrons and holes reduces the efficiency of energy exchange between these two species. The carrier system may then approach thermal equilibrium with the lattice system so that both systems can be characterized by the same quasi-equilibrium temperature. The non-equilibrium optical phonons then decay into acoustic phonons. At this stage, energy may be partially removed from the initial excitation area by traveling coherent acoustic phonon (CAP) waves [90, 91, 92]. Eventually, by recombination and thermal diffusion processs, the system may return to equilibrium.

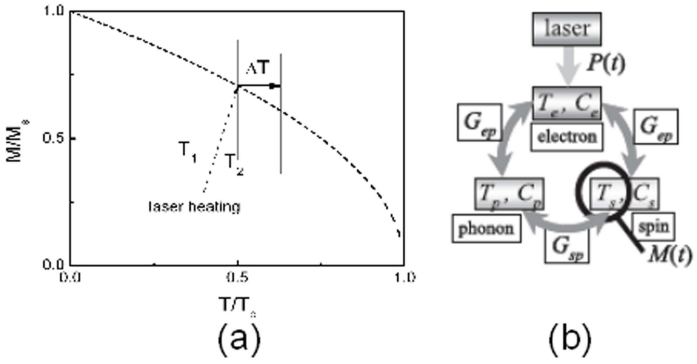

Figure 4.1: Schematic representation of the laser heating effect.

From the above descriptions, it can be seen that the photo-excitation (or photo-absorption) in a semiconductor system leads to transition of the original equilibrium temperature T_1 to an elevated temperature T_2. Obviously, this phenomenon can be

applied to other material systems (e.g. ferromagnetic metals, magnetic semiconductors). In a ferromagnetic system, from the Landau theory of ferromagnetism [70], we know that the magnetization **M** is a function of temperature T, and magnitude of the magnetization decreases as temperature increases. So the photo-excitation of a ferromagnetic material results in a reduction of magnetization. This process is called *demagnetization*, which is schematically shown on figure 4.1.

4.3 Dynamics of traveling coherent acoustic phonon and its detection

As mentioned in section 4.2, the relaxation of photo-excited carriers in semiconductors involves the emission of traveling coherent acoustic phonons (CAPs). In these experiments, femtosecond pump light pulses are absorbed at the sample surface, leading to the generation of the traveling CAPs. The traveling CAP wave can be classically described and modeled by a traveling strain pulse [93]. In general, the laser pulse changes the electron and phonon distribution functions $f_e(k)$ and $f_l(k)$ by $df_e(k)$ and $df_l(k)$, respectively. These changes produce a stress that is given by [94]

$$\sigma_{ij} = \Sigma \frac{\partial E_k}{\partial n_{ij}} df_e(k) + \Sigma \frac{\partial \hbar\omega_k}{\partial n_{ij}} df_l(k), \tag{4.1}$$

where E_k and ω_k are the electron energy and the phonon frequency with wave vector k, respectively. If the electrons and phonons are in local thermal equilibrium and thus both temporal behaviors can be described a single temperature, their contributions to the strain can not be distinguished. This process generally appears on the order of a few picoseconds [95]. So the propagating CAP can be viewed as a strained layer moving away from the surface with longitudinal acoustic phonon velocity V_s.

In this application of pump-probe technique, the CAP wave is characterized by the interference between the probe beams reflected from the air/bulk interface and the bulk/strained layer boundary at the distance $z(t) = V_s t$ from the surface (see figure 4.2). The reflectance in the three layer system is [96]

$$R = |\frac{r_{12} + r_{23}e^{2i\kappa z}}{1 + r_{12}r_{23}e^{2i\kappa z}}|^2, \tag{4.2}$$

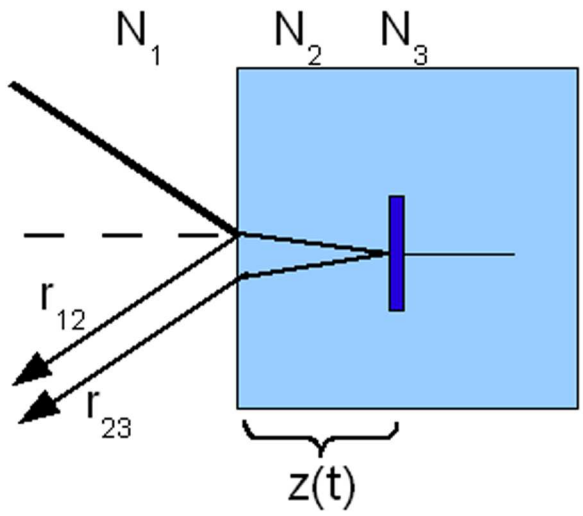

Figure 4.2: A schematic representation of CAP wave creation can be characterized using a pump-probe technique.

where $r_{ij} = (\hat{N}_i - \hat{N}_j)/(\hat{N}_i + \hat{N}_j)$ is the Fresnel reflection amplitude from the boundary between media i and j, and $\hat{N}_i$ is the complex refraction coefficient in media i. Here $\hat{N}_1 = 1$ in air, $\hat{N}_2 = \hat{N}(\omega) = n(\omega) + i\kappa(\omega)$ in the bulk semiconductor, $\hat{N}_3 = \hat{N}(\omega) + \delta\hat{N}(\omega)$ in the strained layer, and $k = (\omega/c)\hat{N}\cos\theta$ is the normal component of the wave vector in the bulk. Thus, we define r_{12} as the reflection amplitude from the air/top-layer boundary, and $r_{23} \approx \delta\hat{N}/\hat{N}$ describes the reflection from the moving strained layer. Since the strain-induced change in refraction index, $\delta\hat{N}$, is small, a simple expression for R can be obtained by expanding Eq.(4.2) in the first order in small parameter r_{23}. The differential reflection,$\Delta R/R_0 = (R - R_0)/R_0$, with $R_0 = |r_{12}|^2$, $r_{12} = \rho_{12}e^{i\phi_{12}}$, and $r_{23} = \rho_{23}e^{i\phi_{23}}$, then takes the form [97]

$$\frac{\Delta R}{R_0} \approx 2\rho_{12}\rho_{23}\sqrt{1 + \rho_{12}^4 + \rho_{12}^2\cos(2\phi_{12})}e^{-t/\tau}\sin(2\pi t/T + (\varphi_0 + \varphi_{12} + \varphi_{23})), \quad (4.3)$$

$$\frac{\Delta R}{R_0} \approx Ae^{-t/\tau}\sin(2\pi t/T + \varphi_{init}), \quad (4.4)$$

where A is the amplitude, T is the period, and φ_{init} is the initial phase, which includes phase shifts φ_j(j=0, 12, 23) from the top layer, reflection coefficients r_{12} and r_{23},

respectively. A and T are given by

$$A \propto |\frac{\delta \hat{N}}{\delta \eta_{33}}| \propto |\frac{\delta \hat{N}}{\delta E_g}\frac{\delta E_g}{\delta \eta_{33}}| \propto \sqrt{(\frac{\delta n}{\delta E_g})^2 + (\frac{\delta \kappa}{\delta E_g})^2}|\frac{\delta E_g}{\delta \eta_{33}}|, \tag{4.5}$$

$$T = \frac{\lambda}{2nV_s \cos\theta}, \tag{4.6}$$

where η_{33} is the z component of strain tensor, E_g is the bandgap, λ is the probe wavelength, n the index refraction of the material, and θ is the incident angle of the probe light in the bulk semiconductor. The phase shifts φ_{12} and φ_{23} are given by

$$\varphi_{12} = \sin^{-1}\frac{(1+|r_{12}|^2)\cos(\phi_{12})}{\sqrt{(1+|r_{12}|^4)+2|r_{12}|^2\cos(2\phi_{12})}}, \tag{4.7}$$

and

$$\varphi_{23} = arg(r_{23}). \tag{4.8}$$

The damping time is defined as

$$\tau = \frac{\lambda}{4\pi\kappa V_s \cos\theta} = \frac{Tn}{2\pi\kappa}, \tag{4.9}$$

where the imaginary part of the complex refraction index κ of the bulk semiconductor is related to the absorption coefficient by $\alpha = 2\omega\kappa/c$.

The penetration depth is proportional of the reciprocal of the absorption coefficient. The amplitude of the oscillations depends linearly on the strain-induced change in the refraction coefficient. The latter is determined by a local reduction of the bandgap δE_g due to a lattice expansion in the strained layer.

4.4 Coherent Spin (Magnetization) Dynamics

4.4.1 Undamped Larmor precession

Consider the situation where a general external magnetic field $\vec{B} = (B_x, B_y, B_z)$ is applied to a single spin system $\vec{s}$, the Hamiltonian is given by $H = -\vec{\mu}\cdot\vec{B} = g\mu_B\vec{s}\cdot\vec{B}$. Under the Heisenberg picture, the equation of motion can be expressed as

$$\frac{dA}{dt} = \frac{1}{i\hbar}[A, H], \tag{4.10}$$

where A is any physical observable and explicitly depends on time. If A is replaced by the spin $\vec{s}$, the equations of motion for a single spin system are given by

$$\frac{ds_x}{dt} = \frac{g\mu_B}{i\hbar}(s_z B_y - s_y B_z), \tag{4.11}$$

$$\frac{ds_y}{dt} = \frac{g\mu_B}{i\hbar}(s_x B_z - s_z B_x), \tag{4.12}$$

$$\frac{ds_z}{dt} = \frac{g\mu_B}{i\hbar}(s_y B_x - s_x B_y), \tag{4.13}$$

where g and μ_B are the spectroscopic splitting factor and Bohr magneton, respectively.

In the derivation of the above equations, the commutation relations for the Pauli operators are used and are expressed as $[\sigma_i, \sigma_j] = 2i\sigma_k$, where i, j and k describe the permutations of x, y and z.

Defining the Larmor precession vector as $\vec{\Omega} = \frac{g\mu_B \vec{B}}{\hbar}$, the above equations of motion for a single spin system can be expressed as

$$\frac{d\vec{s}}{dt} = \vec{\Omega} \times \vec{s}. \tag{4.14}$$

If one classically considers a torque $\vec{T} = \vec{\mu} \times \vec{s}$ acting on spin $\vec{s}$, one obtains a similar equation. Generally, the gyromagnetic ratio $\gamma = g\mu_B/\hbar$ is often used and is equal to 176 Ghz/T (2.21×10^5 Hz/(A/m)). Extending the equation of motion of a single spin to a multi-spin system, denoted by the magnetization vector $\vec{M}(\vec{r}, t) = \frac{\Sigma \vec{\mu_i}}{\Delta V_r}$, we end up the following precessional motion of the magnetization $\vec{M}$,

$$\frac{\partial \vec{M}}{\partial t} = -\gamma \vec{M} \times \vec{B}. \tag{4.15}$$

An instantaneous perturbation of the magnetization or of the magnetic field will thus result in a precession of the magnetization around a magnetic field. With a zero damping force, that is, disallowing any relaxation mechanism, the precession will continue indefinitely while the system remains at a constant energy level. However, in real experiments energy dissipation always takes place. It is always phenomenologically described by some damping parameters that can be obtained by tracing the temporal behavior of $\vec{M}$. The detail microscopic nature of this dissipation process is

not understood [98]. The following sections provide insight into how to add a variety of dissipation terms into an otherwise non-dissipation model.

4.4.2 Landau-Lifshitz and Landau-Lifshitz-Gilbert equations

Landau and Lifshitz in 1935 were the first to propose a dynamic model for the precessional motion of magnetization (macro-spin system) [84]. In the model, not only the external magnetic field is considered but also the presence of quantum mechanical effects and anisotropy are also taken into account by phenomenologically introducing the effective field $\vec{H}_{eff}$, which is given by

$$\vec{H}_{eff} = \vec{H}_{ex} + \vec{H}_{an} + \vec{H}_{m} + \vec{H}_{ext}, \tag{4.16}$$

where $\vec{H}_{ex}$, $\vec{H}_{an}$,$\vec{H}_{m}$, and $\vec{H}_{ext}$ are the fields from exchange interaction, anisotropy, magnetostatic interaction, and external contributions, respectively. Using this, the Landau-Lifshitz equation corresponding to equation (4.15) is derived to be

$$\frac{\partial \vec{M}}{\partial t} = -\gamma \vec{M} \times \vec{H}_{eff}. \tag{4.17}$$

In order to introduce dissipation into the system, an additional term proportional to $\vec{M} \times (\vec{M} \times \vec{H}_{eff})$ is added. This term describes the relaxation of magnetization to a stable energy minimum. This additional term tends to force the magnetization $\vec{M}$ to turn towards the direction of the effective field $\vec{H}_{eff}$. When the system is not in equilibrium, the damping term will pull the magnetization to the equilibrium direction which is parallel to the direction of the effective magnetic field. Therefore, this damping term points perpendicular to the precessional torque and magnetization and can be written as

$$\vec{D}_1 = \frac{\lambda}{M_s} \vec{M} \times (\vec{M} \times \vec{H}_{eff}), \tag{4.18}$$

where $\lambda(> 0)$ is the parameter which characterizes the damping, and M_s is the saturation magnetization. Then the Landau-Lifshitz equation becomes

$$\frac{\partial \vec{M}}{\partial t} = -\gamma \vec{M} \times \vec{H}_{eff} - \frac{\lambda}{M_s} \vec{M} \times (\vec{M} \times \vec{H}_{eff}). \tag{4.19}$$

Gilbert [85] in 1955 introduced another form of phenomenological damping term into the Landau-Lifshitz equation which is derived under the framework of a Lagrangian formulation. This term is expressed as

$$\vec{D}_2 = \frac{\alpha}{M_s}(\vec{M} \times \frac{\partial \vec{M}}{\partial t}), \tag{4.20}$$

where $\alpha(> 0)$ is the Gilbert damping coefficient, whose magnitude only depends on the material.

Combing Eqs. (4.17) and (4.20), one can arrive at the so-called Landau-Lifshitz-Gilbert (LLG) equation

$$\frac{\partial \vec{M}}{\partial t} = -\gamma_L \vec{M} \times [\vec{H}_{eff} - \frac{\alpha}{M_s \gamma_L} \frac{\partial \vec{M}}{\partial t}]. \tag{4.21}$$

The relationship between Landau-Lifshitz equation and LLG equation can be understood by rewriting equation (4.21) in the form of equation (4.19)

$$\frac{\partial \vec{M}}{\partial t} = -\frac{\gamma_L}{1+\alpha^2} \vec{M} \times \vec{H}_{eff} - \frac{\gamma_L \alpha}{(1+\alpha^2) M_s} \vec{M} \times (\vec{M} \times \vec{H}_{eff}). \tag{4.22}$$

One can immediately notice that the Landau-Lifshitz model and the LLG model are equivalent mathematically if one assumes that

$$\gamma = \frac{\gamma_L}{1+\alpha^2}, \lambda = \frac{\gamma_L \alpha}{(1+\alpha^2)} = \gamma_L \alpha. \tag{4.23}$$

It is important to note that both additional terms assume that the magnetization magnitude is constant such that $|\vec{M}| = M_S$.

4.4.3 Bloch-Bloembergen equation

The Landau-Lifshitz or LLG model describes the actual dynamics of real magnetic systems quite successfully. However, this model cannot accurately deal with the magnetization dynamics where there is a reduction in $|\vec{M}|$. This reduction is generally caused by excited magnetic states (higher magnons or spin wave) during the precession or reversal of the magnetization [99]. One possible model is described by the Bloch-Bloembergen equation [86, 87]

$$\frac{\partial M_x}{\partial t} = -\gamma(\vec{M} \times \vec{H}_{eff})_x - \frac{M_x}{T_2}, \tag{4.24}$$

$$\frac{\partial M_y}{\partial t} = -\gamma(\vec{M} \times \vec{H}_{eff})_y - \frac{M_y}{T_2}, \tag{4.25}$$

$$\frac{\partial M_z}{\partial t} = -\gamma(\vec{M} \times \vec{H}_{eff})_z - \frac{(M_z - M_s)}{T_1}, \tag{4.26}$$

where two different damping times are introduced into the equation of motion: the longitudinal relaxation time T_1, i.e., the irreversible direct dissipation of energy into the system, and the so-called transverse relaxation time T_2, which describes dephasing of the spin-system and generation of magnons at a constant energy level. Two extreme cases are interesting: (a) in the limit of small angle approximation, the magnetization $|\vec{M}|$ can be regarded as constant when $T_1 = 2T_2$; (b) If $T_1 >> T_2$, the projection of M onto the z axis remains constant, since the precessional energy is transformed into the transverse components M_x and M_y. A schematic representation describing both the Landau-Lifshitz and the Bloch-Bloembergen models are shown in figure 4.3.

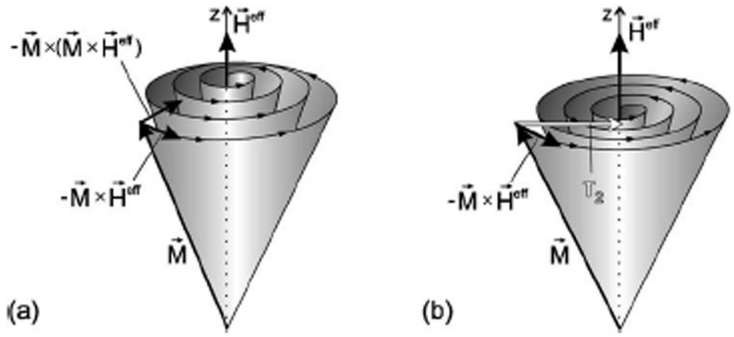

Figure 4.3: (a) Landau-Lifshitz model and (b) Bloch model

4.5 Magnetic energy

Now let us turn to the Eq. (4.16). As we know, the effective field is given by gradient of the magnetic energy of a given system [28]. Therefore, it is helpful to take into account the magnetic energy. In fact, the magnetic energy can be categorized into exchange energy, anisotropy energy, magnetostatic energy, and Zeeman energy.

The exchange energy, corresponding to the exchange field, is an approximate representation of the quantum mechanical exchange interaction. In the Heisenberg

model, the energy density between any two atoms i and j with spins $\vec{S_i}$ and $\vec{S_j}$ is given by $U = -2J\vec{S_i} \cdot \vec{S_j}$. Here J is the exchange integral, and is related to the overlap of the charge distribution of the atoms i and j. The charge distribution, quantum mechanically, is partially represented by the angular momentum number L. That means a different L results in a different charge distribution in the system. From the Pauli principle, any two electrons cannot have the exact same quantum numbers. Each quantum number set (S, L) represents a certain energy state of the system. Thus, the electrostatic energy of a multiple spin systems will depend on the relative orientation of the spins; the difference in energy defines the exchange energy.

Magnetic anisotropy is the direction dependence of a material's magnetic properties. A magnetically isotropic material has no preferential direction for its magnetic moments in zero field, while a magnetically anisotropic material will align its moment to the so-called easy axis. In the easy axis direction, the magnetic energy of the system is minimized. There are several types of magnetic anisotropy:(1) magnetocrystalline anistropy, (2) stress anisotropy, (3) shape anisotropy, and (4) exchange anisotropy. Magnetocrystalline anisotropy originates from the spin-orbit coupling between the spins and the lattice in the material. The crystal structure introduces preferential directions for the magnetization. Theoretically, it needs to be calculated from the electronic structure of the material. For example, in a cubic crystal with magnetization $\vec{M} = (M_x, M_y, M_z)$, the energy is given by

$$e(\hat{M}) = K_{1c}(\hat{M}_x^2\hat{M}_y^2 + \hat{M}_x^2\hat{M}_z^2 + \hat{M}_y^2\hat{M}_z^2) + K_{2c}(\hat{M}_x\hat{M}_y\hat{M}_z)^2, \tag{4.27}$$

where $\hat{M}(= \vec{M}/M)$, K_{1c}, and K_{2c} are unit vector, first order and second order cubic anisotropy constants, respectively. The easy axis direction is determined by minimizing the energy $e(\hat{M})$. As a consequence of the magnetocrystalline anisotropy, once the magnetization is aligned with an easy direction, work must be done to change it. In order to switch from one easy axis to another, the magnetization has to overcome an energy barrier, which is the difference between the energy in the easy direction and that in the intervening hard direction. In addition to the cubic anisotropy, there are

many other types of crystal anisotropies. One important anisotropy arises from uniaxial structure symmetry. Its corresponding energy is characterized by the uniaxial anisotropy constant.

Because the exchange energy strongly depends on the detailed interaction between neighboring atoms, variations in atomic positions, strain, will strongly influence the magnetic interaction. Stress induced anisotropy gives rise to a single easy axis, and thus leads to uniaxial anisotropy. It is important to note that in the ferromagnetic (Ga,Mn)As system under compressional strain, the detailed origin of the uniaxial anisotropy is still being debated [100].

Shape anisotropy is due to the non-perfect spherical shape of a magnetic particle, where the demagnetization field will not be equal in all directions. This leads to energy minimization in certain directions. Demagnetization arises from an internal field induced by "surface monopoles" due to the initial magnetization. A schematic picture of this effect is shown in Figure 4.4.

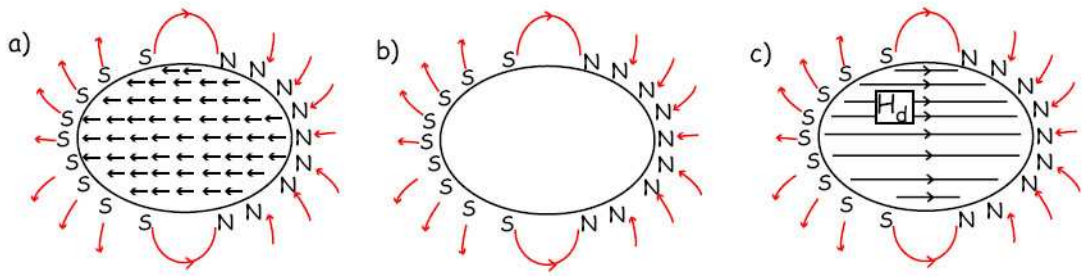

Figure 4.4: (a) Internal magnetizations within a ferromagnetic crystal; (b) Creation of an identical external field from the surface monopoles; (c) The internal "Demagnetizaion field" resulting from the surface monopoles.

The concept of exchange anisotropy or exchange bias [101] is relatively new, and occurs inside bilayers (or multilayers) of magnetic materials. This class of anisotropy causes a shift in the soft magnetization curve of a ferromagnetic film. It is believed that the magnetic properties at the interface determine the exchange anisotropy [102].

However, many important issue in both experiment and theory are still in question [103].

When a magnetic moment is placed in a magnetic field, it has energy associated with this field depending on orientation. This energy can be described by $E_m = -\vec{M} \cdot \vec{H}$. If the magnetic field is from magnetostatic interaction, this energy is called magnetostatic energy. If the field is applied externally, this energy is called Zeeman energy. This energy is minimized when the magnetization $\vec{M}$ is aligned with the field $\vec{H}$. The magnetization in a single domain is uniform, and applying the external magnetic field does not change the amplitude of the magnetization, but will tend to rotate the magnetization direction toward the field. This rotation generally is not energy free, and needs to surmount a certain energy barrier in order to rotate, due to the above mentioned anisotropy properties.

4.6 Experimental Results and Discussions

4.6.1 Ultrafast Phonon Dynamics in GaMnAs/GaAs structures

As previously mentioned, the introduction of III-V diluted magnetic semiconductors (DMSs) has opened up promising opportunities to combine semiconducting properties and robust magnetism into conventional electrical and optical devices, leading to the future development of spin-based devices [27, 28]. (Ga,Mn)As is a good example and is regarded as a benchmark material [28, 74]. Despite many time-domain carrier and spin dynamics studies that have been done on (III,Mn)V structures over the years, no systematic time-resolved experiments on phonon dynamics have been attempted. A recent paper [91] reported pronounced coherent acoustic phonon (CAP) oscillations in GaSb with an InMnAs capping layer, which, however, only played the role of generating coherent phonons. In this thesis, we focus on acoustic phonons traveling in (III,Mn)V structures which are shown to reveal important properties of these materials.

Coherent acoustic phonons have been generated and detected in many other ma-

terial systems using ultrafast spectroscopy. It has shown itself to be a very effective technique to unravel equilibrium and non-equilibrium carrier and phonon dynamics [93, 104, 105, 97, 106, 107]. In this approach, an incident ultrafast (femtosecond) optical pump pulse is absorbed on a sample surface resulting in the generation of a coherent acoustic phonon pulse, which subsequently propagates in the material at the sound velocity. The resulting phonon pulse modifies locally the dielectric constant of the material. This modification is detected by introducing another optical probe pulse. Finally, the ultrafast transient reflectivity spectroscopy measurements are realized by systematically adjusting the delay.

Here, we discuss the femtosecond optical pump excitation of ultrafast coherent phonons generated in a thin over-layer of gold. The subsequent CAP wave (strain pulse),which alters locally the optical properties, propagates in the $Ga_{1-x}Mn_xAs$/GaAs and is detected by monitoring the reflected probe pulse. The ferromagnetic $Ga_{1-x}Mn_xAs$ thin layer is grown by a low temperature molecular beam epitaxy (LT-MBE) method. For the samples studied, electron beam evaporation was used to deposit a 5 nm thick film of gold on top of the $Ga_{1-x}Mn_xAs$ in order to generate acoustic waves by optical excitation. Here, we focus primarily on the $Ga_{1-x}Mn_xAs$ (x = 0.024) sample, with a Curie temperature $T_C \approx 30$ K. Similar results were observed for other samples with Mn concentrations (x=0.018,0.023). All the studied $Ga_{1-x}Mn_xAs$ thin films have a thickness $\sim 1\mu m$.

All our pump-probe experiments measuring transient reflectivity changes $\Delta R/R$ were performed at a temperature of 10 K, employing a Ti:Sapphire laser with a repetition rate of 76 MHz, which produces ∼150 fs-wide pulses. Both pump and probe beams were focused onto the sample at the same spot with a diameter of around 100 μm and an intensity ratio of 10:1. The pump light typically had a fluence of 1.7 $\mu J/cm^2$.

Figure 4.5 shows the transient reflectivity signal $\Delta R/R$ measured in the sample at 10 K with Mn concentration x=0.024. The inset is the measured oscillatory response,

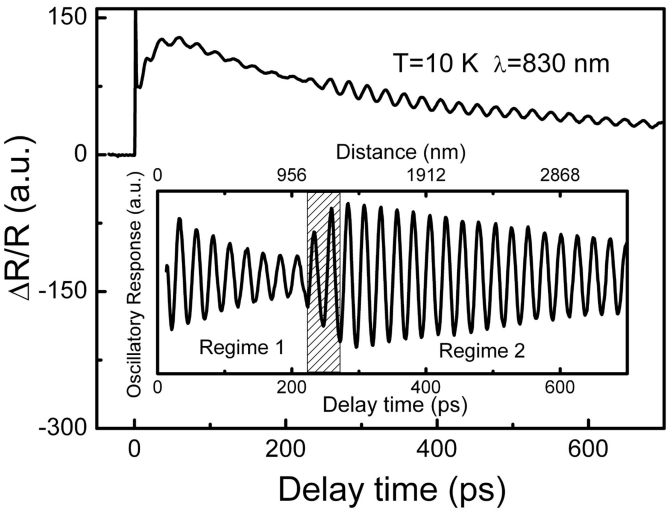

Figure 4.5: Pump-probe response of $Ga_{0.976}Mn_{0.024}As$/GaAs at 10 K for 830 nm. Inset: the subtracted oscillatory response divided into three regimes: regimes 1 and 2 with damped oscillations, and transitional regime indicated by the shadow area.

which is obtained by subtracting the thermal relaxation background. Both pump and probe pulses are centered at 830 nm, with a photon energy somewhat below the band gap of GaAs (∼817 nm). It can be seen that the total response consists of a fast transient (on the order of a few picoseconds) followed by a tail superimposed by two distinct damped oscillatory regimes, separated by a narrow transition region. The initial fast transient is typical of the electronic contribution to the pump-probe signal.

In order to determine whether the oscillations originate from ferromagnetism in the $Ga_{0.976}Mn_{0.024}As$, an external magnetic field of 0.15 T was applied. No changes in the period of the oscillations were observed. Thus, the oscillatory behavior is not due to a magnetically related mechanism. However, the observed oscillations may be explained by a propagating strain pulse model [93]. In this model, an ultrafast pump pulse absorbed at the surface of the film gives rise to a transient electron and phonon temperature increase within the illuminated area, which sets up a transient thermal and/or electronic stress at the sample surface. This stress induces a strain pulse (coherent longitudinal acoustic phonon), which propagates away from the surface at the speed of sound. This strain pulse alters the local optical properties, namely, the

dielectric constants or the refractive index, and creates a discontinuity. When the time-delayed probe pulse penetrates into the sample, the light is partially reflected from the top surface, and the rest of the transmitted light reaches the strain pulse inside, partially reflecting due to the discontinuity in the optical properties. As the coherent phonon wave travels, the top sample surface and the strain pulse surface act as an interferometer. Oscillations arise from the fact that the distance between the two surfaces is constantly changing, causing a periodic phase difference between the two reflected beams. It is clear that the wavelength of the pump light plays little role in creating phonon waves, as long as the top layer can absorb the photon-excitation energy. The reflectivity change $\Delta R/R$ for the oscillatory behavior and its period T take the forms Eqs. (4.4) and (4.6), respectively.

The thickness of the top gold layer is small (5 nm), so that we assume the entire Au layer is excited to generate the CAP wave. The generated CAP wave first travels through $Ga_{0.976}Mn_{0.024}As$ along the normal direction at the speed of the longitudinal acoustic phonon (LAP) $V_{s(\mathrm{GaMnAs})}$ before it reaches GaAs. After that, it continuously propagates into the GaAs with LAP speed $V_{s(\mathrm{GaAs})}$. We estimate that it takes about Δt ($\approx$ 210 ps) for the strain wave to reach GaAs layer if assuming that $V_{s(\mathrm{GaMnAs})}$ is approximately equal to $V_{s(\mathrm{GaAs})}$ (4.78×10^3 m/s at 10 K [108]). It can be seen from experimental results that 210 ps is around the transition region between the two distinctive damped regimes. So we may reasonably conclude that the two oscillatory regimes 1 and 2 represent propagation of the strain wave inside the $Ga_{0.976}Mn_{0.024}As$ and GaAs layers, respectively. When the photon energy is less more than 1.59 eV ($\sim$780 nm), the oscillations damped very fast and could not be found in regime 2.

We performed wavelength dependent studies of the oscillations near the bandgap of GaAs(see Figure 4.6). It can be seen that oscillations in $Ga_{0.976}Mn_{0.024}As$ decay markedly at all the wavelengths studied. In contrast, the GaAs oscillatory response may persist for very long times at probe wavelengths below the bandgap of GaAs. Applying Eq.(4.4) separately to the two regimes with damped oscillations, we can nu-

merically fit our experimental data at different wavelengths. Some fitted parameters as a function of wavelength (or photon energy) are given in Figure 4.7.

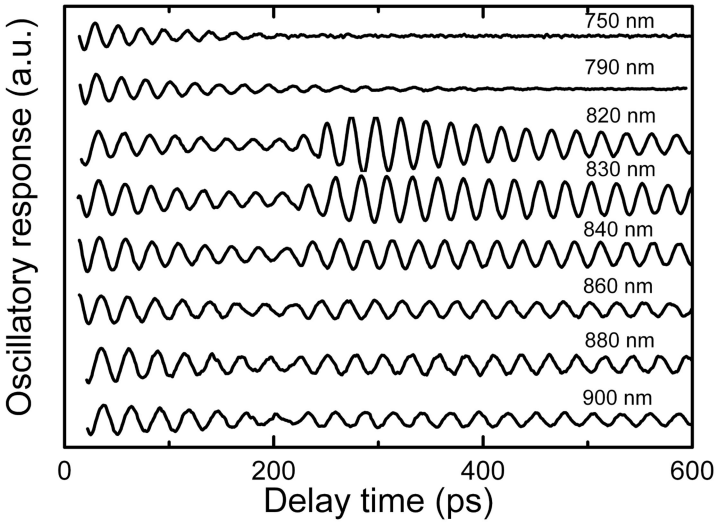

Figure 4.6: Temporal profiles of subtracted oscillatory response for different wavelengths at 10 K.

Figure 4.7(a) shows that the oscillation periods for both materials are close to linear versus the probe light wavelength, in good agreement with Eq.(4.6). This agreement between experiment and theory confirms that the oscillations are only the result of traveling CAPs propagating through $Ga_{0.976}Mn_{0.024}As$ and GaAs layers continuously. It can be seen from Fig. 4.7(a) that the period in $Ga_{0.976}Mn_{0.024}As$ is systematically larger than the period in GaAs at the wavelengths around the bandgap of GaAs. However, the change is astonishingly small (less than 2%) compared to the large doping levels ($\sim 10^{20}$ cm^{-3}). As we know, the speed of LAP waves propagating along [100] is given by $V_s = (C_{11}/\rho)^{1/2}$ for zincblende-structure materials with elastic constant C_{11} and density ρ. In the as-grown $Ga_{1-x}Mn_xAs$ ($x > 0.01$) sample, considering the primary substitutional Mn_{Ga} and the $\sim 20\%$ interstitial Mn_I [28], its density is roughly the same as that of GaAs. If we further assume that $Ga_{1-x}Mn_xAs$ has the same elastic constant as GaAs [109], the LAP velocity V_s of $Ga_{1-x}Mn_xAs$ approximately equals that of GaAs. Therefore, our results, together with Eq.(4.6),

indicate that introducing Mn into GaAs leads to a reduction in the refractive index $n(\omega)$ compared to that in GaAs. A kink-like feature in $n(\omega)$ profile of GaAs expected by $T(\lambda)$ curve was also demonstrated by previous work [110]. On the other hand, a theoretical computation of $n(\omega)$ in $Ga_{1-x}Mn_xAs$ is non-trivial. First, the real or imaginary components of the dielectric constant $\epsilon(\omega)$ over a wide spectral range should be calculated. Then, using the Kramers-Kronig relations, detailed information of $n(\omega)$ can be obtained. Especially, in first-principle calculations, the electronic structure of $Ga_{1-x}Mn_xAs$ needs to be known so as to derive the interband and intraband contributions to the dielectric constant $\mathrm{Im}[\epsilon(\omega)]$ or $\mathrm{Re}[\epsilon(\omega)]$ [111].

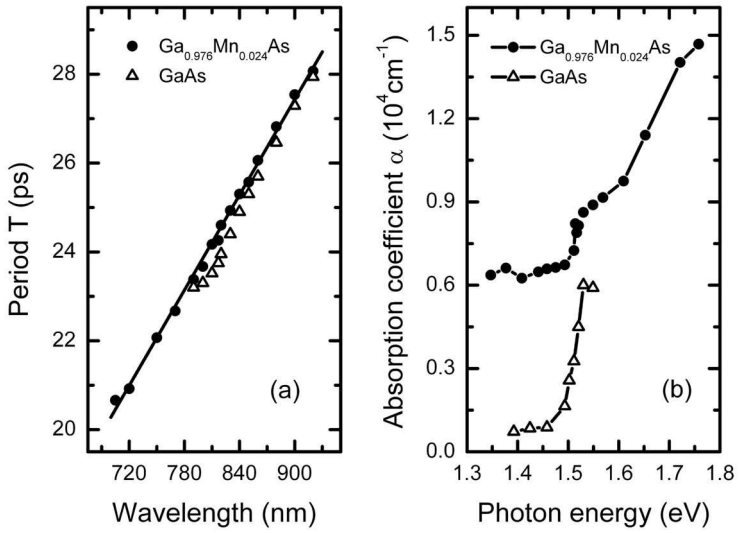

Figure 4.7: (a) Oscillation period T as a function of wavelength λ for GaAs (open triangle) and $Ga_{0.976}Mn_{0.024}As$ (dot). Solid straight line is a linear fit of experimental data for $Ga_{0.976}Mn_{0.024}As$. (b) Absorption coefficient α as a function of photon energy for $Ga_{0.976}Mn_{0.024}As$ (line+dot) and GaAs (line+open triangle).

Another experimental result is that the absorption coefficient α can be directly obtained from our measured damping time τ. Analysis of the absorption resonance/band of $\alpha(\omega)$, attributed to different interband or intraband transitions, may reveal the electronic structure of the ferromagnetic $Ga_{1-x}Mn_xAs$, which has been an important and lively issue over the last several years [28]. Fig. 4.7(b) shows our experimental absorp-

tion coefficient α in terms of different photon energies for $Ga_{0.976}Mn_{0.024}As$ and GaAs provided that $V_s = 4.78 \times 10^3$ m/s. As expected, for GaAs it was clearly seen that a sharp step-like absorption feature happens around 1.51 eV, below which α quickly drops close to zero. This observation is in agreement with canonical characteristics of a band model for GaAs with a direct band gap. In contrast, $\alpha(\omega)$ for $Ga_{0.976}Mn_{0.024}As$ changes rather smoothly in the whole spectral range studied. Especially, no strong abrupt variation was observed at around the bandgap of GaAs. The absorption coefficient below 1.51 eV is still very large and stays almost constant ($\sim 0.66 \times 10^4$ cm^{-1}) down to 1.34 eV. The big difference in the light absorption between the ferromagnetic $Ga_{1-x}Mn_xAs$ and the GaAs can be due to the LT-MBE growth technique, where large unintentional defects such as As_{Ga} antisites and Mn_I interstitials acting as double donors are introduced except the main substitutional Mn_{Ga}. These donor levels provide additional excitation energy levels in the band structure, and lead to the strong broadening of the gap and absorption edge [28]. Our measurements imply that ferromagnetic $Ga_{1-x}Mn_xAs$ has a very different electronic structure and optical properties than those of GaAs. This method, in principle, can be further employed to directly get the information of $n(\omega)$ and $\alpha(\omega)$ in the $Ga_{1-x}Mn_xAs$ system by measuring the period and damping time of the oscillations in the visible, mid-infrared or far-infrared spectra range, and provide an alternative way to understand the band structure of this material in more detail.

From Figs. 4.5 and 4.6, it is clearly seen that at wavelengths close to the GaAs bandgap (a) the oscillation amplitude as a function of wavelength for GaAs suddenly increases, and (b) in the time domain the oscillation amplitudes experience abrupt changes when the strain pulse traveling from $Ga_{0.976}Mn_{0.024}As$ to GaAs. To interpret the results, we note that the strain pulse (η_{33}) can induce a small perturbation δEg to the bandgap E_g and the absorption coefficient α behaves like a sharp step function in terms of photon energy in the GaAs semiconductor. So $\frac{\partial \hat{N}}{\partial E}$, especially $\frac{\partial \kappa}{\partial E}$, for GaAs around $E_g + \delta E_g$ can experience a rapid change as the photon energy E passes through

the absorption onset. According to Eq. (4.5), in the vicinity of the bandgap the amplitude A for GaAs manifests itself a strong peak shown in Fig. 4.6. As also discussed above, the absorption coefficient α for ferromagnetic $Ga_{1-x}Mn_xAs$ varies smoothly in the wavelength range studied. Thus, the change in $\frac{\partial \hat{N}}{\partial E}$ for $Ga_{0.976}Mn_{0.024}As$ around $E_g+\delta E_g$ is much smaller compared to that of GaAs. As a result, when the strain pulse propagates across the $Ga_{0.976}Mn_{0.024}As$/GaAs interface, the amplitude of the oscillations exhibit sudden increases for photon energies around the bandgap of GaAs. This method may be employed to determine unknown film thickness or the longitudinal speed of sound, given that one of them is known.

Finally, we turn to the transition regime in the temporal oscillatory response as shown in Figs. 4.5 and 4.6. At wavelengths around the GaAs bandgap, the width of this regime in the time domain is roughly 45 ps, corresponding to a traveling distance of the strain pulse of about 200 nm. The oscillation amplitude in this region increases gradually as time increases. We therefore suspect the existence of a transition region between $Ga_{0.976}Mn_{0.024}As$ and GaAs substrate. Actually, before depositing the studied $Ga_{1-x}Mn_xAs$ samples, a 100 nm LT-GaAs buffer layer is grown at low temperature (LT) conditions ($\sim$270 °C) following a normal ($\sim$600 °C) 100 nm GaAs buffer layer on GaAs (100) substrate. Due to the As_{Ga} antisite defects in LT-GaAs, the amplitude of the oscillatory response due to the strain pulse in the LT-GaAs and GaAs is expected to be different around the GaAs bandgap. At the same time, the residual Mn ions inside the chamber lead to the incorporation of a few Mn impurities into these two GaAs buffer layers. Moreover, during growth of $Ga_{1-x}Mn_xAs$, the Mn on the top could also back-diffuse into these two GaAs buffers. Therefore, all these factors might together provide reasonable explanations for the gradual increase of the amplitude in the transition regions. Nevertheless, the analysis of the oscillation amplitudes provides a sensitive way to detect changes in the material along the growth direction in heterostructure systems.

4.6.2 Photoinduced Coherent Spin Dynamics in GaMnAs systems

In past years, ultrafast nonequilibrium and dynamic properties of a wide variety of magnetically ordered systems have been investigated, and have provided useful insights into the future application of novel magnetic devices [24, 112, 113, 114]. Especially, ferromagnetic semiconductors such as (III,Mn)V systems have attracted intense interest because of their potential for the spintronics applications due to carrier-mediated ferromagnetism arising from the interaction between itinerant carrier spins and localized magnetic moments [27, 28]. Recently, using ultrafast pump-probe magneto-optical spectroscopy, several research groups have reported a wide variety of collective magnetic phenomena in (Ga,Mn)As [77, 30, 76, 78, 79, 82, 114, 115, 116]. The observed magnetization dynamics may be divided into two regimes in terms of time evolution of the photoexcited (Ga,Mn)As system: femtosecond (or subpicosecond) and picosecond (to nanosecond). In the subpicosecond regime, depending on the photoexcitation strength, much research has focused on light-induced demagnetization and thermal/non-thermal influence on magnetization [114, 117, 118, 83]. The dynamics of coherent carrier and Mn spins have also been treated in the picosecond to nanosecond regime [77, 30, 76, 78, 79, 82, 114, 115, 116]. In this regime, a recently observed phenomenon is the precession of ferromagnetically coupled Mn spins (magnetization) due to light-induced magnetic easy axis reorientation. In both regimes, the interpretations of many of the experimentally observed phenomena remain a matter of intense debate. Many of these issues revolve around questions of whether the effects are of thermal or non-thermal origin.

In order to address these issues, we have carried out comprehensive temperature and photo-excitation intensity dependent measurements of photo-induced magnetization precession in $Ga_{1-x}Mn_xAs$ with no externally imposed magnetic field. By comparing and contrasting the temperature and intensity dependence of the precession frequency, damping, and amplitude, we identify important light-induced nonlinear effects and obtain information on the relevant physical mechanisms. Our measure-

ments of photo-induced magnetization show coherent oscillations, arising from the precession of collective Mn spins. That the amplitude of the magnetization precession saturates above a certain pump intensity is a strong indication that the direction of the magnetic easy axis remains unchanged at temperatures above about half the Curie temperature (T_C). The precession may be explained by invoking an ultrafast change in the orientation of the in-plane easy axis, due to an impulsive change in the magnetic anisotropy induced by the laser pulse. We find that the Gilbert damping coefficient, which characterizes the Mn-spin relaxation, depends only weakly on the ambient temperature but changes dramatically with pump intensity. Our results suggest a general model for photo-induced precessional motion and relaxation of magnetization in the (Ga,Mn)As system.

The (Ga,Mn)As sample is grown by molecular beam epitaxy (MBE) using a Riber 32 R&D MBE machine at the University of Notre Dame. Firstly, a semi-insulating "epi-ready" (001) GaAs substrate is heated to 600 °C under As flux for deoxidation. After heating and thermal cleaning, a GaAs buffer layer is grown on the substrate at normal GaAs growth conditions (∼600 °C) in order to obtain an atomically flat surface. Following this, another layer of GaAs will be grown on the GaAs buffer layer, this time under low temperature conditions to prepare the sample for incorporation of Mn into the final layer (∼290 °C). As mentioned previously, a low temperature growth MBE (LT-MBE) method must be employed to alleviate the problems of low solubility and precipitation of Mn under normal growth conditions. Finally, with the incorporation of Mn, a layer of (Ga,Mn)As is grown under the same low temperature conditions. Our $Ga_{1-x}Mn_xAs$/LT-GaAs(buffer)/GaAs(buffer) samples, with Mn concentration x from $\sim$ 0.01 to $\sim$ 0.073, can be divided into three main categories in terms of layer thickness: (a) ∼95 nm/2 nm/100 nm, (b) ∼300 nm/100 nm/100 nm, and (c) ∼1000 nm/100 nm/100 nm. Depending on the annealing conditions, they can be categorized into as-grown samples and annealed samples with different annealing temperatures. The Curie temperature in these Mn incorporated layers T_C

varies from $\sim 5K$ to $\sim 110K$. The detail optical setup used for the pump-probe experiments is described in Chapter 2. The pump and probe beams either have the same photon energy or are tuned to be different by putting BBO crystal in the pump (or probe) path to double the photon energy. The pump beam which is perpendicular to the sample can be adjusted to have a linear, right-circular (σ+), or left-circular (σ-) polarization with a typical fluence of $I_0 = 0.75\ \mu$ J/cm^2 (up to $\sim 10\ \mu$J/cm^2). The probe beam is linearly polarized and near perpendicular to the film to detect magnetization dynamics via measuring the Kerr rotation angle (θ_K) or the Kerr ellipticity (ε_K). All the experiments were carried out with no applied external magnetic field except where noted.

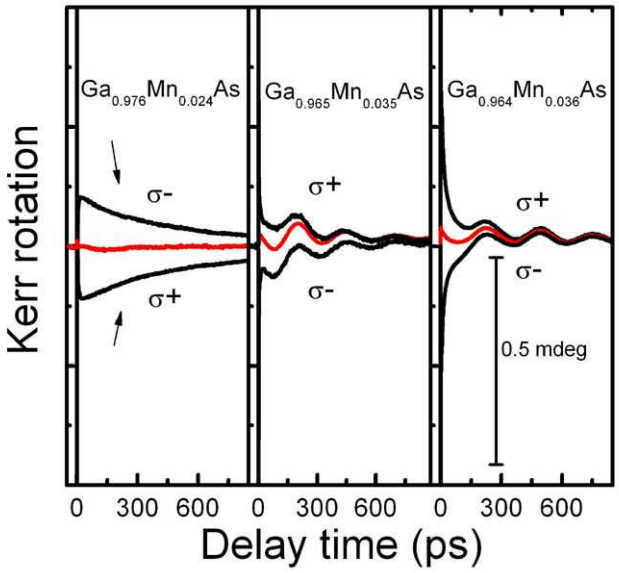

Figure 4.8: Time-resolved Kerr rotation data with respect to the excitation by linearly-polarized and circularly polarized light (σ+ and σ-) at 10 K with photon energy 1.57 eV for three ferromagnetic GaMnAs samples corresponding to sample categories (a), (b), and (c), respectively. The red curve arises from excitation by linearly polarized light.

Time-resolved magneto-optical Kerr effect (TRMOKE) Measurements were car-

ried out, where the pump and probe beams were at the same wavelength. Fig. 4.8 shows a typical time-resolved magneto-optical Kerr effect (TRMOKE) measurement with photon energy 1.57 eV above the GaAs bandgap E_g ($\approx$1.53 eV at 10 K) at low temperatures for $Ga_{1-x}Mn_xAs$. It can be clearly seen that the temporal Kerr rotation signals are almost symmetric in the long time domain (order of $\sim$1 ns) with respect to the right- and left-circular polarized photoexcitation. Similar profiles were previously reported by other groups [78, 79]. Instead, in the curves corresponding to excitation by linear polarized light, as shown in Fig. 4.8, we obtained an oscillatory behavior with a period on the order of 100 ps superimposed on a tiny exponential decay signal. The oscillations are also superimposed on the signals arising from circularly polarized light excitation. The phase difference between the oscillations for each sample is close to zero (see also Ref. [30]), which implies that if the excitation light is modulated between left- and right-circular polarizations, the oscillation can be totally eliminated. This was confirmed in our experiment by putting a photoelastic modulator (PEM) in the pump beam (see also 4.10 [119]. From observation of the data shown in Fig. 4.8, the near symmetric and the oscillatory signals arise from sources which are decoupled. The circular-polarization dependent curves were also found to persist at all studied temperatures (up to 295 K). In contrast, the oscillatory behavior only existed at temperatures below the Curie temperature T_C (See Fig. 4.9). Additionally, due to the optical selection rules around the bandgap in GaAs system, the Kerr rotation reflecting coherent carrier spin dynamics is expected to be dependent on polarization of the excitation laser pulse [5, 120]. At the same time, the lifetime of coherent hole spins is ultrashort (femtoseconds) due to strong spin-orbit scattering on top of valence band [121].

Based on the above discussion, we attribute the above nearly symmetric signals to light-induced coherent electron spins in the conduction band of the studied Mn-doped GaAs systems. As a part of this study, we carried out temperature dependent measurements of coherent electron spins in the conduction band, where the pump

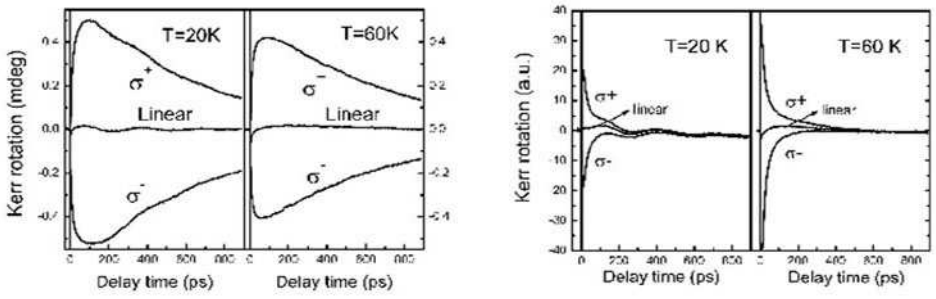

Figure 4.9: Kerr rotation measurements for $Ga_{1-x}Mn_xAs$ with x = 0.036 (Category (a)) and x = 0.035 (Category (b)) excited by linearly-polarized and circularly polarized light (σ+ and σ-) at two temperatures 20 K and 60 K. In both cases the photon energy is 1.57 eV. Oscillations due to magnetization precession are superimposed on the decay curves measured at 20 K. No oscillations are observed at 60 K.

beam was modulated by a PEM. One example is shown in figure 4.10. We can fit the experimental curves by two exponentially decaying components [77]. The relaxation rate was found to vary little at temperatures around T_C, but to decrease rapidly near room temperature. This can be seen in Fig. 4.10. The almost constant relaxation time around T_C is consistent with what was reported in Ref. [77]. However, Figs. 4.8 and 4.9 show that the carrier spin lifetime and Kerr rotation signals measured using different samples can be drastically different for different pump polarization. The longest spin lifetime we observed is around 100 ps at room temperature in several samples. The physical mechanism is still not clear.

As opposed to the carrier spin phenomena, the observed oscillatory behavior can only arise from the coherent Mn spins in the ferromagnetic $Ga_{1-x}Mn_xAs$ samples. The magnetic origin of the oscillations is confirmed by the measurements showing the overlap of the pump-induced rotation and ellipticity through the entire time scan range (See Fig. 4.12). To understand this experimental result, it is useful to recall the different stages of time evolution of the (Ga, Mn)As system following photoexcitation [83]. Initially, an ultrashort laser pulse creates excited carriers with a well-defined coherent phase relationship. These coherent states may quickly become decoherent

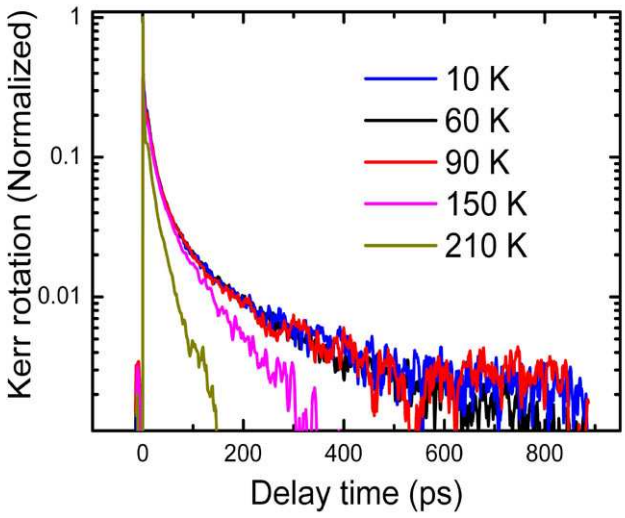

Figure 4.10: Temporal Kerr rotation profile excluding the oscillatory behavior in terms of different ambient temperatures at sample $Ga_{0.964}Mn_{0.036}As$ annealed at 286 °C (Category (a)).

(on a femtosecond time scale) due to scattering processes between carriers involving electron-electron, hole-hole, and electron-hole scattering. During these scattering processes, the distribution function of the excitation cannot be characterized by a temperature, although the total excess energy of the carrier system is conserved. Due to scattering among carriers, the energy of the carrier system is redistributed leading to the creation of a hot carrier Fermi-Dirac distribution on a sub-picosecond time scale. Thereafter, the emission of phonons increases rapidly due to the carrier-phonon interaction, which plays a major role in the exchange of energy between carriers and the lattice. The carrier system transfers its excess energy to the lattice primarily in the form of optical phonons within a few picoseconds followed by decay to acoustic phonons. Before equilibration, the temperature characterizing the thermalized distribution function of carriers is higher than that of the lattice system. At this stage, the whole photoexcited system can be phenomenologically described by an effective temperature (carrier $T_{e/h}$ and lattice T_l) and a specific heat (carrier $C_{e/h}$ and lattice C_l). Then, the carrier system begins to equilibrate with the lattice system, which leads to the same quasi-equilibrium temperature for both systems. By recombination

and thermal diffusion processes, the system finally returns to equilibrium.

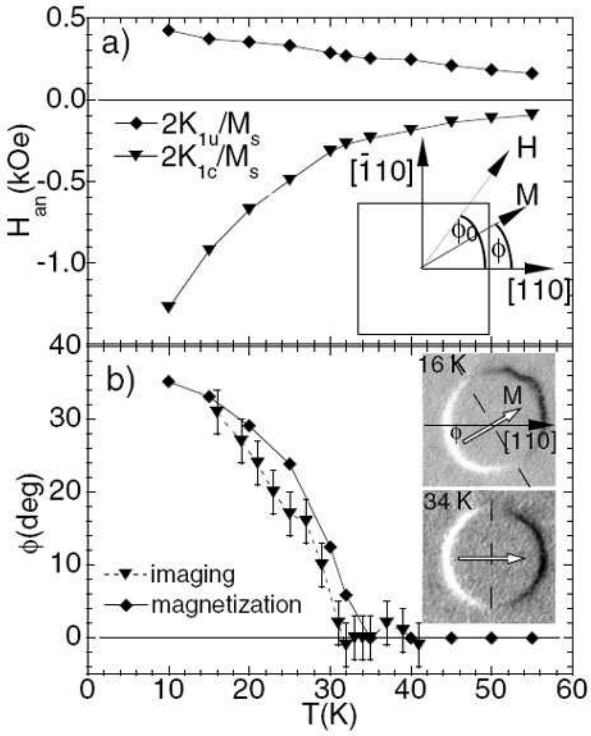

Figure 4.11: (a) Temperature dependence of the uniaxial and cubic anisotropy fields (in the sample plane). The inset defines the experimental geometry. (b) Temperature dependence of the angle of the easy axis with respect to the [110] direction. The inset shows the magneto-optical contrast around an 80-μm hole at 16 and 34 K, which identifies the moment orientation at H=0.

In the ferromagnetic $Ga_{1-x}Mnx$As/GaAs system, it is important to note that following excitation both the early time nonthermal (as described above) and later time thermal (or quasithermal) excited regimes, the magnetic anisotropies can be different as compared to the ground state. This may be due either to the nonthermally photoexcited holes (Δp) [122, 100], or to the temperature elevation (ΔT) [123]. Below the Curie temperature T_C, the magnetic equilibrium position (easy axis) is in-plane, determined by an angle Φ in respect to [110] direction, depends on the interplay between the in-plane uniaxial anisotropy constant K_u and the first order cubic anisotropy constant K_{c1}. At very low temperatures, Φ is close to $\pi/4$ ([100] direction). In contrast,

Φ approaches to zero ([110] direction) when the ambient temperature exceeds about $T_C/2$ [123] (see Fig.4.11). After the optical excitation, the new angle of the easy axes is then given by $\Phi = \Phi[K_{c1}(T_0 + \Delta T(t), p_0 + \Delta p(t)), K_u(T_0 + \Delta T(t), p_0 + \Delta p(t))]$, where T_0 and p_0 are the initial (ambient) temperature and hole concentration. Therefore, the easy axis may quickly assume a new direction following photoexcitation if $\Delta T(t)$ or $\Delta p(t)$ is sufficiently strong. This transient change in the magnetic easy axis triggers a precession of ferromagnetically coupled Mn spins (magnetization) around a new effective magnetic field, and leads to oscillatory behavior in the TRKR signal. Oscillations with relative long periods ($\sim$ 100 ps) seen in the TRMOKE measurements were observed before by several groups [79, 30, 115, 116]. However, whether $\Delta T(t)$ or $\Delta p(t)$ plays the key role evoking the oscillation is still an important issue.

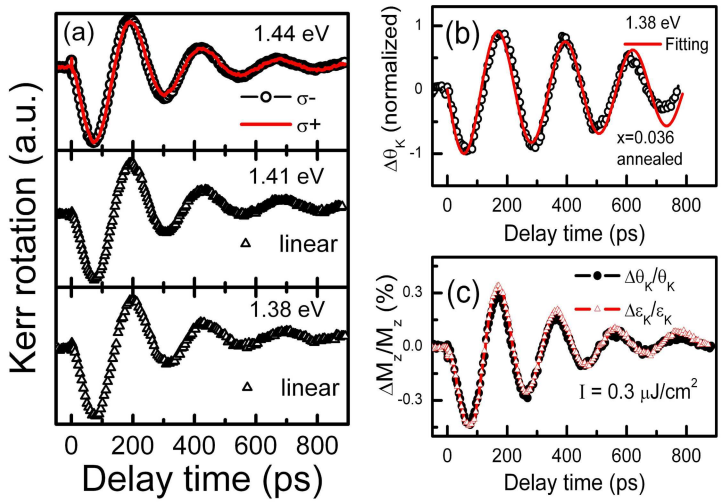

Figure 4.12: (a) Temporal Kerr rotation profiles measured at photon energies below bandgap of GaAs at 10 K for sample $Ga_{0.965}Mn_{0.035}As$ (Category (b)); (b) TRKR signal at 10 K with E_{ph} = 1.38 eV for sample $Ga_{0.964}Mn_{0.036}As$ (Category (a)); (c) Transient Kerr rotation and Kerr ellipticity signals at photon energy E_{ph} = 1.38 eV for sample $Ga_{0.965}Mn_{0.035}As$ (Category (b)) with a constant pump fluence $I_0/2$.

Previously, all observations reported on the magnetization precession were obtained using photon energies E_{ph} larger than the GaAs bandgap E_g via the one-color pump-probe scheme. Here, we also covered the spectral range below E_g. Typical

TRKR profiles below E_g are shown in Fig. 4.12 for two $Ga_{1-x}Mn_xAs$ samples at 10 K. Fourier transform of the oscillation indicates only single precessional mode existing. The signal can be fitted well by the equation,

$$\Delta\theta_K = A\exp(-t/\tau_d)\sin(\omega t + \phi). \tag{4.28}$$

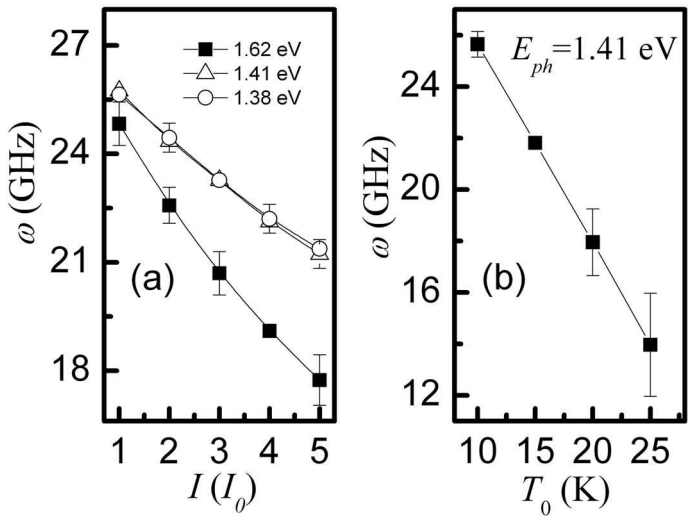

Figure 4.13: (a) Numerically fitted precession frequency ω as a function of pump fluence I at 10 K at different photon energies for sample $Ga_{0.965}Mn_{0.035}As$ (Category (b)); (b) Precession frequency ω as a function of ambient temperature T_0 at photon energy $E_{ph} = 1.41$ eV with a constant pump fluence I_0.

These measurements clearly demonstrate that with the same external conditions (except E_{ph}) only pure oscillatory behavior is observed. Importantly, all the carrier spin related dynamics in the long time domain disappears. For $E_{ph} < E_g$, no electrons are excited to the conduction band, and hence no Kerr rotation signal from the net coherent electron spins is obtained. This observation confirms our interpretation that the polarization-dependent signal in Fig. 4.8 is due to the photoexcited electrons. The oscillations observed in Fig. 4.12 are related to intraband light absorption. In GaMnAs samples grown by the LT-MBE method, no distinct optical absorption bandgap has been identified. This may be attributed to (a) the presence of defect states within the band gap (such as As_{Ga} antisites and Mn_I interstitials),

(b) the breakdown of momentum conservation due to disorder, and (c) free carrier absorption [28, 124]. In this case, light absorption perturbs the hole distribution in the valence bands by exciting or introducing additional itinerant holes via electron intraband transitions to localized defect states, and thus leads to the observed magnetization precession. Clearly, exciting the system with the photon energies below E_g can eliminate the TRKR signal due to the photoinduced carrier spins in the long time domain for all polarizations of the pump light. We also note that the amplitude A of oscillations has no strong dependence on the probe polarization direction, which indicates the polar Kerr rotation dominates the detected TRKR signal and the contribution due to the magnetic linear dichroism [125] can be neglected. This excitation regime is therefore useful for studying the precession of coherent Mn spins. We carried out pump intensity and temperature dependent measurements on the oscillatory behavior to see the possible difference of the effects evoked by excitation with E_{ph} varying below or above the GaAs bandgap. Figs. 4.13(a) and (b) show the fitted oscillation frequency for the as-grown $Ga_{0.965}Mn_{0.035}As$ (Category (b)) as a function of pump influence (I) and ambient temperature (T_0), respectively. It can be seen that the precession frequency ω decreases with increasing either the pump intensity or the ambient temperature. This indicates that transient temperature rise induced by the photoexcitation may play important role causing the oscillatory behavior. In Fig. 4.13(b), another result is that the precession frequency for $E_{ph} > E_g$ is larger than that for $E_{ph} < E_g$ at the corresponding pump fluences. Besides, with I increasing, ω decreases much faster for $E_{ph} > E_g$ compared to that for $E_{ph} < E_g$. We also notice that for $E_{ph} < E_g$ the frequency at 10 K with excitation intensity $5I_0$ roughly equals one at 15 K with pump fluence I_0. Thus, an estimation of the average light-induced temperature increase can be made to be $\Delta T \sim 1$ K under the conditions: $T_0 = 10$ K and $I = I_0$. This causes a $\sim$3% change of anisotropy constants [123], which is a small perturbation to the system. The optically induced instantaneous increase of temperature can also be estimated by $\Delta T = \Delta E/(C_m \Delta m)$, where ΔE is the pulse energy,

C_m is the heat capacity, and the Δm is the mass of the illuminated volume. The small perturbation leads to small fluctuation of the magnetization ($|\vec{M}(t)| \approx Const$) at low pump fluences. So in the mean field approximation the phenomenological Landau-Lifshitz-Gilbert (LLG) equation can be employed to describe the collective magnetization dynamic in our experiments. The LLG equation is written as

$$\frac{\partial \vec{M}}{\partial t} = -\gamma \vec{M} \times \vec{H}_{eff} + \frac{\alpha}{M} \vec{M} \times \frac{\partial \vec{M}}{\partial t}, \tag{4.29}$$

where $\vec{M}$ is the local Mn magnetization, γ is the gyromagnetic ratio, $\vec{H}_{eff} = -\partial E/\partial \vec{M}$ is the effective field given by the gradient of magnetic energy E, and α is the Gilbert damping coefficient. The effective field $\vec{H}_{eff}$ includes the external static, magnetic anisotropy, and exchange fields [28]. The first term on the right hand side (rhs) of Eq. (4.29) describes the precession behavior of the magnetization, and the second term represents the relaxation of collective magnetization motion. Fig. 4.14 shows the measured Gilbert damping coefficient in samples $Ga_{0.964}Mn_{0.036}As$ (annealed at 286 °C) and $Ga_{0.965}Mn_{0.035}As$ (as-grown). It is clearly seen that α in the annealed sample is much smaller (about ten times) than that in the as-grown sample. A similar result was also observed in FMR experiments [126].

Since in this case there is no external applied magnetic field, within the mean field treatment of the *p-d* magnetic exchange interaction, the average Mn spin $< \vec{S} >$ precesses around an effective magnetic field $\vec{H}_{eff}$, which is mainly attributed to the anisotropy field $\vec{H}$ and the hole-spin mean field $\beta < \vec{s} >$. The dynamics of the average hole spin $< \vec{s} >$ are determined by its precession around the mean field $\beta N_{Mn} < \vec{S} >$ due to the Mn spins, and by its rapid relaxation due to the strong spin-orbit interaction in the valence band with a rate Γ of the order of tens of femtoseconds [68]. Here, β is the exchange constant. N_{Mn} are the number of Mn_{Ga} per unit volume. Due to the hole spins precessing and relaxing much faster than the changes in the ferromagnetically coupled Mn spins, in the adiabatic limit the interplay between the exchange interaction in Eq. (4.29) and the carrier spin dephasing results gives an important damping contribution [83, 127]. This damping mechanism, arising from

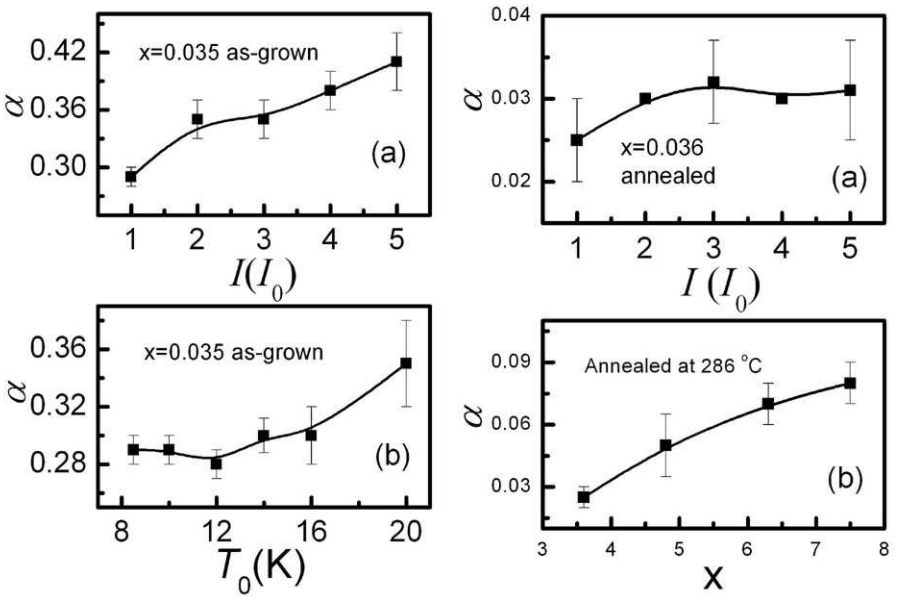

Figure 4.14: (a) Gilbert damping coefficient as a function of pump intensity for the annealed sample; (b) Gilbert damping coefficient as a function of Mn concentration x for the samples annealed at 286 °C; (c)(d) Gilbert damping coefficient for as-grown sample as functions of pump fluence and ambient temperature, respectively.

the *p-d* exchange interaction with itinerent carriers, is believed to be essential to understand the intrinsic relaxation of ferromagnetic (III,Mn)V semiconductors [126]. Therefore, an effective LLG equation in the adiabatic limit can be obtained [83, 127]

$$\frac{\partial \vec{M}}{\partial t} = -\gamma_r \vec{M} \times \vec{H} + \frac{\alpha_r}{M} \vec{M} \times \frac{\partial \vec{M}}{\partial t}, \tag{4.30}$$

where γ_r and α_r include the kinetic-exchange contribution and other damping contributions.

The following expression for the magnetic energy E provides a good explanation of static experiments [28, 123]

$$E(\vec{M}) = \frac{K_{c1}}{2}(\hat{M}_x^2 - \hat{M}_y^2)^2 + K_u(\hat{M}_x - \hat{M}_y)^2 + K_{uz}\hat{M}_z^2, \tag{4.31}$$

where $\hat{M} = \vec{M}/M$, and K_{uz} is the uniaxial anisotropy constant perpendicular to the film. A sufficiently large $K_{uz} > 0$ ensures the magnetic easy axis lies within the sample plane. We therefore use Eqs. (4.30) and (4.31) to present a qualitative

picture about the light-induced precession magnetization dynamics. Due to the initial in-plane magnetization in compressive trained $Ga_{1-x}Mn_xAs/GaAs$ system [123], we can consider a small perturbation with $M_x \approx M$ in the coordinate system with x-y plane parallel and z-axis perpendicular to the sample plane, respectively. Then, Eq. (4.30) is expanded into three components,

$$\frac{\partial M_x}{\partial t} = 0, \tag{4.32}$$

$$\frac{\partial M_y}{\partial t} = -2\gamma_r K_{uz} M_z - \alpha_r \frac{\partial M_z}{\partial t}, \tag{4.33}$$

$$\frac{\partial M_z}{\partial t} = -2\gamma_r K_u - 2\gamma_r K_{c1} M_y + \alpha_r \frac{\partial M_y}{\partial t}, \tag{4.34}$$

where we neglect the second order terms. Considering $K_{c1} < 0$ and $K_{uz} > 0$ [123], the above equations have one solution like

$$M_y = A\cos(\omega t + \varphi)e^{-t/\tau}, M_z = A\eta\sin(\omega t)e^{-t/\tau}, \tag{4.35}$$

where

$$\omega = \gamma_r \frac{\sqrt{-\alpha_r^2(K_{uz}+K_{c1})^2 - 4K_{c1}K_{uz}}}{1+\alpha_r^2}, \tau = \frac{1+\alpha_r^2}{\alpha_r\gamma_r(K_{uz}-K_{c1})}. \tag{4.36}$$

According to Eq. (4.35), we notice that a sin- or cos-like signal with exponential decay characterized by a decay time τ and precession frequency ω can be obtained when measuring magnetization y or z component in the time domain after a small perturbation to the initial magnetic equilibrium state. This is consistent with the above numerical fitting Eq. (4.28). It can be seen that the precession frequency ω is closely related the anisotropy constants (e.g. K_{c1} and K_{uz}, which also directly connect the Gilbert damping coefficient with the exponential decay time. Generally, α_r^2 is much smaller than one (see also Fig. 4.14), and can be neglected in Eq. (4.36).

Eqs. (4.35) and (4.36) can readily account for the observations in Fig. 4.13. Below T_C, it is known that both K_{c1} and K_{uz} monotonically decrease when the temperature increases [123, 69]. Eq. (4.36) indicates ω decreases with reducing K_{c1} and K_{uz}. This

conclusion agrees with the results in Fig. 4.13, where ω becomes smaller as raising T_0 or increasing $\Delta T(t)$ via enlarging pump fluence I. On the other hand, increasing the hole concentration can also decrease K_{c1} [100], leading to the results shown in Fig. 4.13. However, in our experiments, $\Delta p/p_0$ is about three or four orders smaller than $\Delta T/T_0$ in the thermal regimes. Therefore, we can conclude that the transient temperature change plays a major role in accounting for the oscillatory behavior. Actually, even in the case of Δp comparable with p_0, $\Delta T/T_0$ is so large that the magnetization dynamics are already dominated by ultrafast demagnetization and the subsequent magnetization quenching [114], and no oscillations should be expected in the long time domain. When the photon energy E_{ph} is comparable to the GaAs bandgap E_g, in thin GaMnAs samples (less than $\sim$ 300 nm) the incident light can be absorbed not only by the top GaMnAs layer but also by the bottom LT-GaAs, GaAs buffers and GaAs substrate due to the penetration depth on the order of one micron deduced from the absorption coefficient. In this case, the local transient temperature change might be much larger than that with E_{ph} far below E_g. For instance, at E_{ph}=1.63 eV, ΔT is estimated to be $\sim$3 K with T_0 =10 K and $I = I_0$, and three times larger than that at E_{ph}=1.38 eV. This effect may be more significant at large pump fluences. The corresponding oscillation frequency should become smaller. This phenomenon is clearly demonstrated in Fig. 4.13. So our data indicate that the top ferromagnetic GaMnAs layer might be affected by its bottom layers with relative strong photoexcitation at $E_{ph} > E_g$. In order to eliminate such influence in the thin samples (less than about 300 nm), one way is to use small E_{ph} (much smaller than E_g), as illustrated above. Another possible way is to employ two-color technique, where the pump photon with its energy tuned sufficiently high enough to be confined within the GaMnAs layer. It is important to note that when $\Delta T(t)$ increases too much $|\vec{S}(t)|$ cannot be regarded as a conserved value, and LLG model does not apply.

The above frequency behavior as a function of pump intensity or ambient temperature was observed in different ferromagnetic GaMnAs samples such as as-grown

$Ga_{0.975}Mn_{0.035}As$ with $T_C \approx 70K$ (Category (b)) in Fig. 4.15. As can also be seen in Fig. 4.15, the amplitude of the oscillations increases as the ambient temperature decreases or as the pump intensity increases. This result is in accord with the fact that the relative change $\Delta T/T_0$ and $\Delta p/p_0$, which determines the magnitude of $\Phi(t)$ and the photo-induced tilt in the easy axis, increases as T_0 decreases or as the pump intensity I increases. It is important to note that in our experiment the amplitude of the oscillations saturates as the pump intensity exceeds about $8I_0$ at $T_0 = 10K$. Thus, the observed saturation may indicate that the magnetic easy axis is stabilized at pump intensity larger than $8I_0$. We estimated that the increase of local hole concentration $\Delta p/p_0$ is about 0.4%, and the local temperature increase $\Delta T/T_0$ is about 160% using the value of specific heat of 1mJ/g/K for GaAs at pump intensity $\sim 8I_0$. This leads to the transient local temperature $T_0 + \Delta T$ close to $T_C/2$. Our data agree with the previously reported result that the magnetic easy axis is already along the [110] direction for $T_0 + \Delta T$ close to or higher than $T_C/2$ [123].

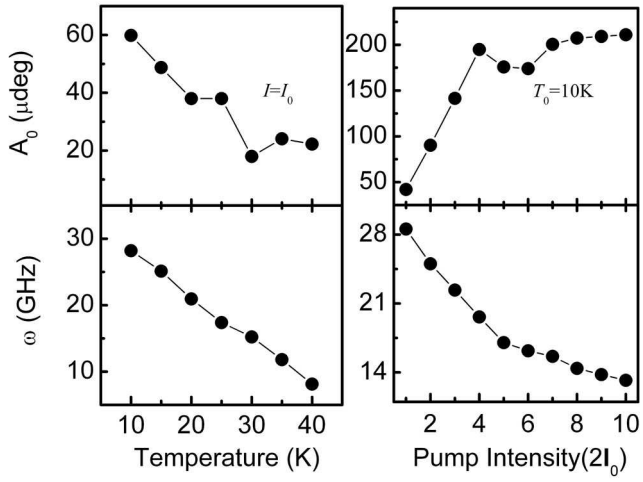

Figure 4.15: Amplitude A and angular frequency ω as a function of temperature T_0 at constant pump intensity $I = 2I_0$; and as a function of pump intensity (in units of $2I_0$) at $T_0 = 10K$.

We now turn to the damping of the oscillations, which is intimately related to lifetime of the excited collective spins. In the hole-mediated ferromagnetic GaMnAs

system, as mentioned above, the spin scattering between the local Mn spins and itinerent hole spins, correlated by the p-d kinetic-exchange interaction, can lead to the relaxation of collective magnetic moments [83, 126, 127]. This gives an intrinsic contribution to the Gilbert damping coefficient. This contribution can be deduced from the adiabatic-limit approximation as (See appendix)

$$\alpha_{pd} = \frac{\gamma s_{\parallel}}{M} \frac{\Gamma_{\perp} h_{eff}}{(h_{eff} + H_{\parallel})^2 + \Gamma_{\perp}^2}, \tag{4.37}$$

where $\Gamma_{\perp}(= 2\Gamma_{\parallel})$ is the hole spin transverse relaxation rate, $h_{eff} = \beta N_{Mn} S$, $s_{\parallel} = \vec{s} \cdot \vec{S}/S$, and $H_{\parallel} = \gamma \vec{H} \cdot \vec{S}/S \approx 0$. In the annealed samples, the Gilbert damping coefficient for TRKR experiments is around 0.03, which is close to the value estimated by Eq. 4.37 [127]. So we anticipate the mechanism due to kinetic-exchange interaction dominates the damping effect [126]. In the annealed samples, we measured α as a function of the pump intensity I and Mn concentration x, respectively (see Fig. 4.14). For the current pump intensity range as mentioned above, the transient increase of local hole density is very small. One would not expect great changes in the parameters of Eq. (4.37), and hence the damping coefficient α_{pd}. This is consistent with the results shown in Fig. 4.14(a). It is also clearly seen that α increases with x increasing. This result, with Mn concentration $x < 8\%$, may be due to the increasing of h_{eff}, which reflects the coupling between exchange interaction and hole density [126]. In contrast, in as-grown samples the Gilbert damping coefficient reaches around 0.3, which is much higher than what the intrinsic kinetic-exchange mechanism expects. So other damping mechanisms must then take over. The most probable mechanism, classically, is the spin dephasing process characterized by T_2, in which the coherent spins, initially precessing in phase, lose their phase due to the spatial and temporal fluctuations of the precession frequencies [86]. These fluctuations are mainly attributed to the local small-scale field inhomogeneities, which are created by such as magnetic defects, domain walls etc.. Quantum mechanically, this dephasing mechanism is mainly explained by the so-called two-magnon scattering [128], where the excited magnon mode (created by photoexcitation) scatters into

other magnons having the same frequency (degenerate magnons) without requiring conservation of the magnon momentum. In as-grown $Ga_{1-x}Mn_xAs$, due to the LT-MBE growth technique, a large number of defects such as As_{Ga} antisites and Mn_I interstitials are introduced. Especially, the local interstitial Mn_I ions are believed to be antiferromagnetically coupled to the main Mn_{Ga} substitutions, which can greatly affect the magnetic properties [28]. Thus, these Mn_I magnetic defects are thought to alter the local magnetic environments, and result in an extrinsic dephasing effect. Removing the Mn_I, perhaps by a post-annealing procedure, should enlarge the magnetization relaxation time. This effect has been demonstrated by our experiments, and by others as well [126]. Besides, our results indicate that this dominated extrinsic mechanism in as-grown samples is relatively independent of the ambient temperature (within a certain range) but largely enhances as increasing the pump intensity (See Fig. 4.14 and also Ref. [30]). If we assume the local precession frequency $\omega(\vec{r},t)$ and the effective field $h[T(\vec{r},t)]$ are temperature dependent, then the dephasing effect is characterized by $\delta\omega$, which is given by

$$\delta\omega = \gamma\frac{\partial h}{\partial T}\frac{\partial T}{\partial r}\delta r + \frac{\partial h}{\partial T}\frac{\partial T}{\partial t}\delta t. \tag{4.38}$$

If the ambient temperature T_0 is kept constant, increasing pump fluence can increase $\partial T/\partial r$ and $\partial T/\partial t$ very efficiently, and hence increase $\delta\omega$, which results in the observed enhancement of dephasing effect. In comparison, $\partial h/\partial T_0$ changes little in a relative temperature range. Up to now, there is still no available theoretical study of the damping mechanism due to distribution of the interstitial Mn_I. However, our experiments indicate that the local temperature distribution connects the extrinsic dephasing effect to the local magnetic Mn_I defect distribution.

Our experimental results in the time domain provide information on the physical factors that contribute to the damping effect. But further experimental and quantitative theoretical work on the damping mechanisms are still needed in the (Ga,Mn)As system. It is important to note that the LLG equation is valid only at low pump intensities. At high pump intensities, an alternative theoretical approach must be

introduced [129]. One approach is using the Bloch-Bloembergen equation (see Eq. (4.24)). Experimentally, one has to measure the magnetization dynamics in three orthogonal directions, in order to determine the exact longitudinal and transverse relaxation rates.

CHAPTER V

Fe/NiO(100) SYSTEM STUDIED BY MSHG

5.1 Introduction

Since the discovery of exchange bias (or anisotropy), i.e., the shift of the hysteresis loop of a ferromagnetic (FM) layer in contact with an antiferromagnetic (AFM) layer in the direction of the applied field [101], numerous investigations have been carried out both from theoretical and experimental points of view due to its widespread application in information storage technology, and due to the intriguing and still not fully understood physics of the problem [102]. Theoretically, there is still little general quantitative understanding of the exchange bias phenomena although several models have been proposed [102]. The models employ different approximation methods. For instance, they only consider ideal interface with intrinsically uncompensated AFM spins. The magnetic couplings are expected to be influenced more significantly by this more than by the presence of low density defective sites.

The interface formed between a ferromagnetic (FM) and an antiferromagnetic (AFM) material has been a subject of study since the discovery of the exchange bias phenomenon[101]. Experimentally, among all the reported investigations involved in insulating AFM materials, such as FeF_2, NiO, CoO, and $Ni_xCo_{1-x}O$ et al., NiO is one very promising candidate for applications[102]. It has advantages of relatively high Neel temperature T_N (525 K), excellent thermal stability and corrosion resistance[130], which makes it attractive for commercial applications. A comprehensive understanding of the chemical and physical properties of the interface is paramount for future applications. Several studies have demonstrated that the Fe/NiO interface is not entirely abrupt since oxygen diffusion takes place resulting in a reduced NiO layer [131, 132]. A structural characterization of the Fe/NiO interface previously conducted by X-ray absorption spectroscopy in combination with density functional calculations has provided evidence that a FeO-like layer is formed

at the interface between the metal and the oxide[133]. As a consequence the magnetic moments of the Fe atoms at the interface are increased. Uncompensated moments coming from the interfacial FeO layer, which may couple ferromagnetically with the Fe layer, are expected to dramatically influence the exchange interaction at the Fe/NiO interface, with deep consequences also for the exchange bias mechanism. Surprisingly, to our knowledge, no investigations using magnetic induced second harmonic generation (MSHG), which is a surface/interface sensitive magneto-optic method, on ferromagnetic metal/antiferromagnetic oxide interfaces have been reported.

5.2 Fe/NiO(100) System

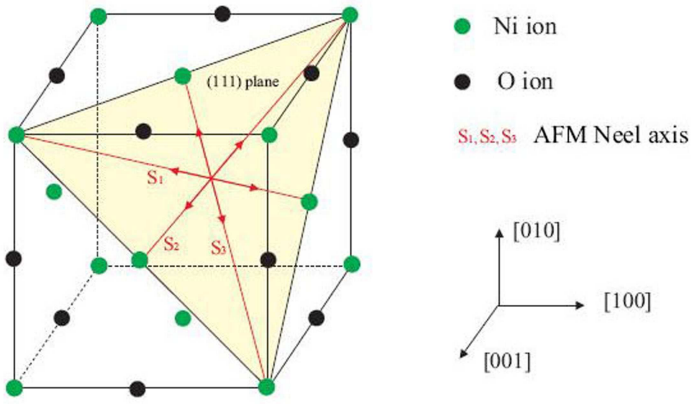

Figure 5.1: Schematically illustrates the lattice and spin structures of NiO single crystal. Here (111) plane is the ferromagnetic sheet indicated as filled plane.

The use of NiO(001) single crystals eliminates the complexity of having small grains with different crystallite orientation. The magnetic properties of anti-ferromagnetic NiO single crystals have been investigated by Roth and Slack by neutron diffraction and optical observations [134, 135]. The Neel temperature of NiO crystal T_N is 525 K, which is significantly higher than room temperature. Above T_N, NiO crystal is paramagnetic. Below T_N, it is anti-ferromagnetic. Its crystal structure is a perfect face center cube (fcc) or rock-salt. The unit cell of NiO crystal is schematically illustrated in Fig. 5.1. The magnetic moments of Ni ions have spin-only values with

S = 12 [134]. The super-exchange interaction between Ni ions on opposite sides of an oxygen ion causes the spins of nickel ions to be aligned antiparallel. The spins of Ni ions are collinear alignment, which are parallel or anti-parallel to the characterized Neel axis. The spins of Ni ions lie within their ferromagnetic (FM) planes [135], shown as the filled (111) plane in Fig. 5.1. Besides (111) FM plane, the NiO crystal has three other possible FM planes, $(\bar{1}11)$, $(1\bar{1}1)$ and $(11\bar{1})$ planes (not shown in Fig. 5.1). The Neel axis of NiO lies within the associated (111) FM plane. It has six-fold symmetry in (111) FM plane, which has three possible Neel axes along [211], [121] and [112] directions denoted as S_1, S_2 and S_3 in Fig. 5.1. The NiO(001) surface can be prepared by cleavage in air of a NiO signal crystal, followed by ultra high vacuum (UHV) annealing at 400 ^{o}C for about half an hour [136]. The use of NiO in the form of films on other material such as Ag and MgO substrates allow us to study the evolution of the properties with increasing thickness. NiO films with a very good crystal quality exposing the (001) surface have already been UHV grown on Ag(001)[133]. MgO is a very stable wide-bandgap material, with application as a support for metal catalysts and as an efficient protective coating material. Similar to the case of NiO, the MgO (001) surface can also be obtained by cleavage in air, followed by UHV annealing at 400 ^{o}C for about half an hour.

Comparing to polycrystalline bilayers, the epitaxial Fe films grown on NiO(001) single crystals have better controlled interface conditions. The lattice constants of fcc NiO(001) single crystal a_{NiO} and bcc Fe film a_{Fe} are 0.4178 nm and 0.287 nm at room temperature, respectively [137]. The lattice mismatch of them $f = \frac{(a_{\mathrm{NiO}}/\sqrt{2} - a_{\mathrm{Fe}})}{a_{\mathrm{NiO}}/\sqrt{2}}$ is about 2.85%, which is relative small and promotes a pseudomorphic growth of Fe film on NiO(001) substrates. Actually, experiments have already shown that Fe can grow epitaxially on NiO(001) with a 45^o in-plane rotation[131]. Some studies on chemistry of the interface show that the reduction of 1$\sim$ML of NiO is induced[131]. Other studies using x-ray absorption technique (XAS) and ab initio density functional theory (DFT) demonstrate that a Fe-Ni alloyed phase on top of an interfacial FeO

planar layer can be formed at the interface[133].

5.3 Experimental Setup

Non-linear optical techniques have been employed to study the interfaces and surfaces of different materials [138, 139]. In particular second harmonic generation (SHG) has proven to be effective in the study of the magnetic state of metal surfaces and thin films [38]. In centrosymmetric media the bulk $\chi^{(2)}$ is zero, but a second harmonic signal can be produced through a higher order term, namely the magnetic quadrupole term. At the surface, the inversion symmetry is broken and SHG takes place. The region where the second harmonic radiation is produced extends few atomic layers around the surface or interface [140]. The magnetization of the surface lowers the surface symmetry can modify the $\chi^{(2)}$ tensor. The susceptibility tensor can be written as a sum of two terms, even and odd in the magnetization. The non-vanishing elements of the susceptibility tensor depend on the symmetry of the investigated surface [38]. As a consequence, by using MSHG it is possible to investigate the magnetization state of the FM film in a region of few ML around a FM/AFM interface. This information is of crucial importance in the understanding of the exchange bias mechanism because the magnetic coupling between the two materials takes place near the interface..

The samples were prepared ex situ in an ultra high vacuum chamber equipped with Ni, Fe and Au evaporating sources, following a well established procedure [136]. The NiO(100) was produced by evaporating Ni in a suitable O_2 atmosphere using MgO (100) as substrate. 10 ML of NiO were deposited in this way. On the freshly prepared NiO surface Fe was deposited at different thicknesses, then 10 nm of Au were deposited as a capping layer to avoid oxidation of the sample. Three different samples were prepared with 2, 5 and 10 ML Fe deposits, respectively. The nickel oxide stoichiometry was verified by X-Ray photoelectron spectroscopy and the epitaxial growth of Fe was checked by low energy electron diffraction. Previous measurements have demonstrated that the capping layer is effective against oxidation induced by air

[141]. For SHG measurements the output beam from a mode-locked Ti:sapphire laser (∼150 fs pulses duration, 800 nm wavelength, 76 MHz repetition rate) was focalized to a spot of about 100 μm at the sample surface (average laser power 190 mW). A Glan-polarizer and a quarter-wave plate were used to obtain a s-polarized beam. The sample was installed in a rotating stage located in the gap of an electro-magnet. The reflected beam coming from the sample passed through a prism to separate the fundamental from the second harmonic response. Two polarizers were used to measure the polarization state of the two beams. The reflected beam intensity was measured by a photodiode whereas the second harmonic intensity was measured by a photomultiplier. The two signals were detected by means of a lock-in amplifier because the pump beam was modulated by an acoustic optical modulator. The detailed setup is shown in Figure 2.4. Before the SHG measurements we verified that a bare MgO substrate produced an undetectable amount of second harmonic signal. Taking into account that the Au capping layer is not magnetic, the magnetic signal comes from only the Au/Fe and NiO(100)/Fe interfaces, and is determined by Eq. (2.6).

5.4 Experimental Results and Discussions

The reported SHG measurements were performed using an s-polarization configuration for the pump laser impinging the sample surface [33]. In Fig. 5.2 the polarization dependence of SHG signal for the 5 ML Fe sample is reported. The two curves are measured by applying two values of magnetic field of 900 Oe, respectively in the longitudinal configuration (see inset in Fig. 5.2), along the [110] direction and clearly show the strong sensitivity of the second harmonic signal to the magnetic state of the surface. In fact, the two polarization patterns are shifted by about 17°, indicating a NOMOKE Kerr angle by far larger than the typical linear MOKE values measured in bulk ferromagnetic metals. For comparison, in Fig. 5.3 the measurement of the fundamental reflected radiation intensity as a function of the polarizer angle is reported for 10 ML Fe on NiO (100). In this case the effect of the magnetic field is hardly

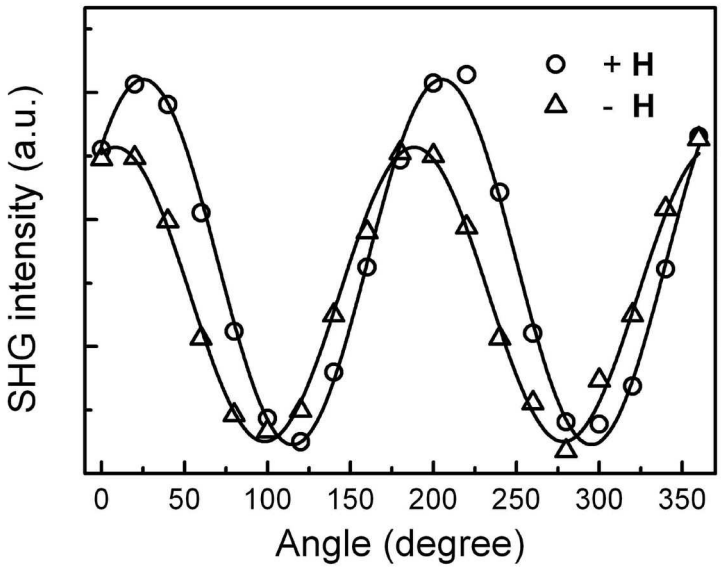

Figure 5.2: Polarization dependence of the SHG measured on the 5 ML Fe sample in longitudinal configuration. The two curves were acquired for the positive (triangles) and negative (circles) magnetization, respectively. The continuous lines are $\cos(\theta)^2$ fitting curves of the experimental points.

detectable demonstrating that the NOMOKE technique is particularly well suited for the investigation of the samples studied in this work. In fact, the linear radiation from the sample is dominated by the light reflected from the Au capping layer. The use of MSHG, then, opens the possibility to easily probe the capped FM/AFM interface.

The evolution of the second harmonic signal as a function of the applied magnetic field was measured by fixing the polarizer angle and by measuring the SHG as a function of the magnetic field. In Fig. 5.4 this measurement is reported for the 5 ML and 10 ML samples. In the two measurements a hysteresis loop is observable. The reported measurements demonstrate that even at this low thickness the iron film is magnetically active.

With appropriate combinations of input and output beam polarizations and geometries it is possible to probe different elements of the susceptibility tensor, thereby obtaining a comprehensive characterization of the interface. We now focus on the

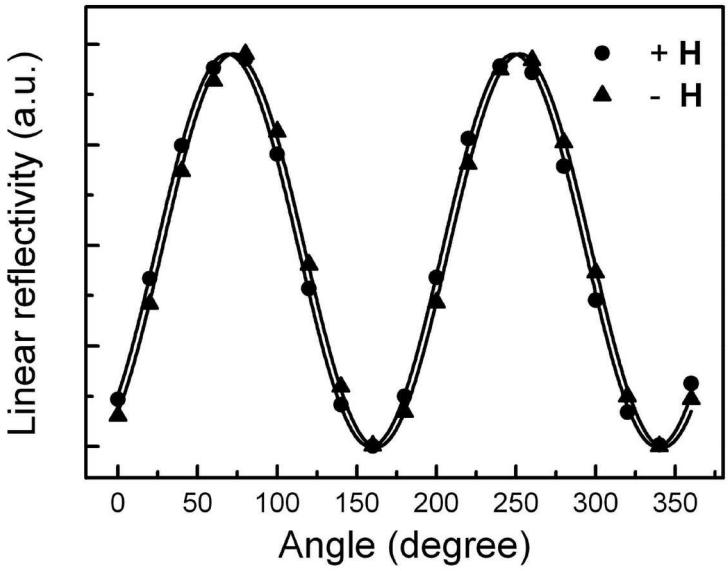

Figure 5.3: Polarization dependence for the reflected beam measured on the 10 ML Fe sample in longitudinal configuration. The two curves were acquired for the positive (squares) and negative (circles) magnetization, respectively. The continuous lines are $\cos(\theta)^2$ fitting curves of the experimental points.

qualitative aspects of the magnetic behavior of the Fe/NiO interface as a function of the metal thickness. Comparing the 5 ML and the 10 ML measurements we notice a strong difference. At high Fe thickness a distinct hysteresis loop is observed, which is a clear signature of ferromagnetic behavior. Decreasing the thickness of the Fe deposit, the hysteresis loop is smaller and is superimposed on a steep background. This behavior can be understood in the light of the structural characterization of the Fe/NiO interface [136]. In fact, the Fe film in the initial stage of the growth is strained on the NiO substrate and about one monolayer is oxidized. The relaxation of the metal film starts at 10 ML, indicating a completely formed metallic film. Below this thickness probably the influence of the oxidized Fe layer at the interface is strong thus resulting in the observed magnetization curve for the 5 ML sample. This picture is confirmed by the measurements at 2 ML reported in Fig. 5.5. In this case an almost undetectable influence of the magnetic field on the SHG polarization depen-

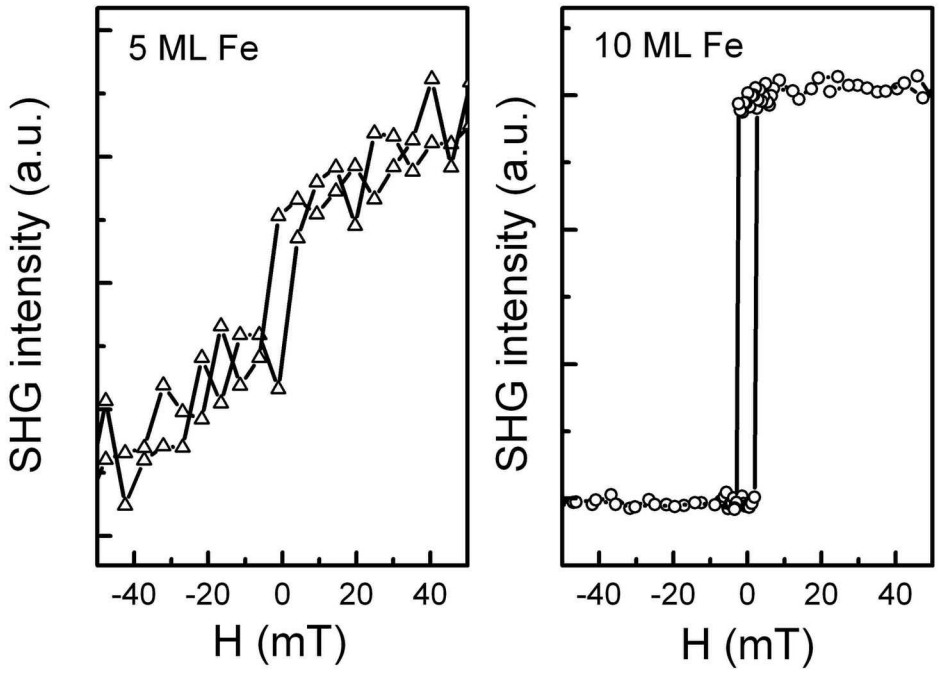

Figure 5.4: SHG measurements as a function of the applied magnetic field, measured for the 10 ML and 5 ML samples, respectively. These curves were acquired for the longitudinal configuration of the magnetic field.

dence is observed. Clearly, at this low thickness the metal film is not ferromagnetic any more. It is arguable that the FeO-like layer formed at the interface presents an AFM character. On the other hand, the formation of super-paramagnetic islands, which would depress the ferromagnetic character of the film at room temperature, appears unlikely in this case because the structural characterization of the 2 ML film evidenced the formation of an epitaxial growth [141].

Interestingly in the 5 ML measurements of the SHG polarization dependence (Fig. 5.2), the magnetic field not only affects the polarization angle but also the intensity of the SHG. As mentioned before in the longitudinal configuration of the magnetic field one should have only a Kerr rotation of the second harmonic beam. A modulation of the intensity is observed in the transversal configuration. A further careful analysis as a function of Fe layer and NiO layer thickness is in progress.

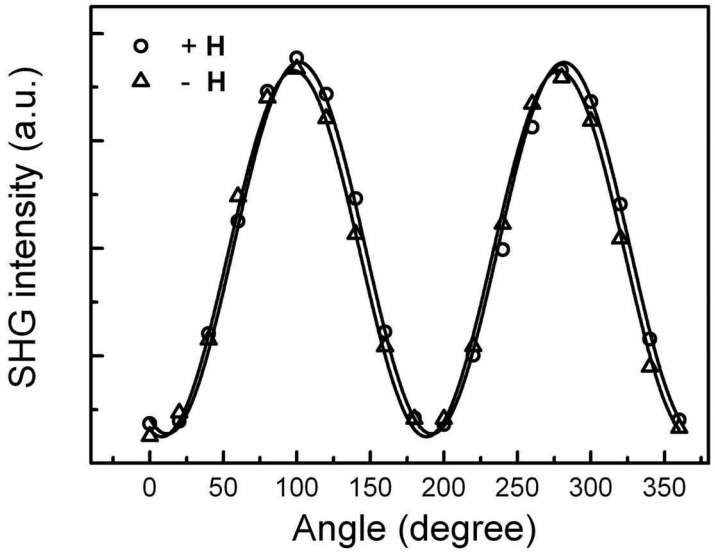

Figure 5.5: Polarization dependence of the SHG measured on the 2 ML Fe sample in longitudinal configuration. The two curves were acquired for the positive (squares) and negative (circles) magnetization, respectively The continuous lines are $\cos(\theta)^2$ fitting curves of the experimental points.

CHAPTER VI

CONCLUSIONS

Using the time-resolved magneto-optical Kerr effect, we observed coherent magnetization precession induced by femtosecond optical pulses in ferromagnetic GaMnAs/GaAs heterostructures. At temperatures below the Curie temperature, we found the coherent oscillations, arising from the local Mn spins, are triggered by an ultrafast photo-induced reorientation of the in-plane easy axis. We demonstrated that the observed magnetization precession damping (Gilbert damping) is strongly dependent on sample annealing conditions and pump laser intensity, but independent of ambient temperature within a certain range. We provided a detailed physical interpretation of the observed light-induced collective Mn-spin precession and relaxation. Oscillatory behavior in the transient reflectivity measurments of these heterostructures is due to coherent acoustic phonons propagating through GaMnAs and GaAs layers. The oscillation period, damping and amplitude are found to be strongly probe photon energy dependent. Changes in the oscillation period, damping and amplitude arising as the phonons travel across the GaMnAs/GaAs interface reflect strong differences in the electronic structures and optical properties of these materials. Analysis of the oscillation amplitude indicates a transition region from GaMnAs to GaAs substrate. Non-linear Kerr rotation measurements have proven to be an effective way to investigate a ferromagnetic/antiferromagnetic Fe/NiO interface. Our measurements demonstrate that the magnetic properties of the studied interface strongly depend on the Fe layer thickness. A clear hysteresis loop is observed only for a thickness greater than 5 ML, whereas for the 2 ML sample the hysteresis loop completely disappears.

APPENDIX A

DAMPING ARISING FROM THE KINETIC EXCHANGE INTERACTION

We derive the effective equation of motion for the collective Mn spins based on the mean-field theory. Since the hole spin precesses and relaxes much faster than the Mn spin, the adiabatic approximation is employed. This means that the hole spin value can be replaced by a steady state value in the reference frame rotating with Mn spin.

The dynamics of average Mn spin $\vec{S}$ can be described by the Landau-lifshitz equation

$$\partial_t \hat{S} = \hat{S} \times \vec{\omega}_{eff}, \tag{1.1}$$

where $\hat{S} = \vec{S}/S$, and $\vec{\omega}_{eff} = \vec{H} - \beta\vec{s}$. $\vec{s}$ is the average hole spin, β is the $p-d$ exchange constant, and H is due to the magnetic anisotropy.

At the same time, the dynamics of average hole spin $\vec{s}$ can be decomposed into dynamics of a component $\vec{s}_\parallel$ parallel to $\vec{S}$ and a component $\vec{s}_\perp$ perpendicular to $\vec{S}$. Only the unadiabatic component $\vec{s}_\perp$ contributes to the Mn spin precession and relaxation. Thus, only the dynamics of $\vec{s}_\perp$ needs to be considered and can be described by [83]

$$\partial_t \vec{s}_\perp = \beta N_{Mn} S \hat{S} \times \vec{s}_\perp - s_\parallel \hat{S} - \hat{S}[\partial_t s_\parallel + \Gamma_\parallel (s_\parallel + s_0)] - \Gamma_\perp \vec{s}_\perp, \tag{1.2}$$

where $\vec{s}_\parallel \parallel \hat{S}$, $\vec{s}_\perp \perp \hat{S}$, and $\vec{s} = \vec{s}_\perp + s_\parallel \hat{S}$.

By projecting the components in Eq.(1.2) parallel and perpendicular to $\hat{S}$, and using the relations $\vec{S} \cdot \partial_t \vec{S} = \partial_t S^2/2 = 0$ and $\vec{s}_\perp \cdot \vec{S}$, we can obtain

$$\partial_t s_\parallel + \Gamma_\parallel (s_\parallel + s_0) = \vec{s}_\perp \cdot \hat{S}, \tag{1.3}$$

and

$$\partial_t \vec{s}_\perp|_\perp = \beta N_{Mn} S \hat{S} \times \vec{s}_\perp - \Gamma_\perp \vec{s}_\perp - s_\parallel \partial_t \hat{S}. \tag{1.4}$$

Assuming a rotating frame with an instantaneous angular velocity $\vec{\omega}$ given by a unit vector $\vec{e}_i$, the rate of change of any vector $\vec{A}$ in the inertial frame then can be

expressed as

$$\partial_t \vec{A} = \partial_t A_i \vec{e_i} + A_i \partial_t \vec{e_i} = \partial_t \vec{A}|_{rot} + \vec{\omega} \times \vec{A}. \tag{1.5}$$

Due to the much slower Mn spin dynamics, we can replace hole spin by its steady state value in the frame of the reference rotating with the Mn spin. Thus, according to Eq. (1.1) the hole spin in the lab frame and rotating frame is related by

$$\partial_t \vec{s}_\perp|_\perp = \partial_t \vec{s}_\perp|_{rot,\perp} + (H_\parallel - \beta s_\parallel)\vec{s}_\perp \times \hat{S}. \tag{1.6}$$

From the Equation (1.1), we can also obtain

$$\vec{s}_\perp \times \hat{S} = \frac{1}{\beta}(\partial_t \hat{S} - \hat{S} \times \vec{H}). \tag{1.7}$$

Then, with $\hat{S} \cdot \partial_t \hat{S} = 0$, the hole spin component $\partial_t \vec{s}_\perp$ can be derived from Equation (1.7) by

$$\vec{s}_\perp = \hat{S} \times (\vec{s}_\perp \times \hat{S}) = \frac{1}{\beta}[\hat{S} \times \partial_t \hat{S} - \hat{S} \times (\hat{S} \times \vec{H})]. \tag{1.8}$$

Combining Eqs. (1.4) and (1.6), and neglecting $\partial_t \vec{s}_\perp|_{rot,\perp}$ under the adiabatic approximation, we can get

$$(\beta N_{Mn} S + H_\parallel - \beta s_\parallel)\vec{s}_\perp \times \hat{S} = -\Gamma_\perp \vec{s}_\perp - s_\parallel \partial_t \hat{S}. \tag{1.9}$$

Inserting Eqs.(1.7) and (1.8) into Eq.(1.9), we obtain

$$(\beta N_{Mn} S + H_\parallel)\partial_t \hat{S} = (\beta N_{Mn} S + H_\parallel - \beta s_\parallel)\hat{S} \times \vec{H} + \Gamma_\perp \hat{S} \times (\hat{S} \times \vec{H}) - \Gamma_\perp \hat{S} \times \partial_t \hat{S}. \tag{1.10}$$

Taking a cross product on both sides of Eq.(1.10) ($\hat{S}\times$Eq.(1.10)), we get

$$(\beta N_{Mn} S + H_\parallel)\hat{S} \times \partial_t \hat{S} = (\beta N_{Mn} S + H_\parallel - \beta s_\parallel)\hat{S} \times (\hat{S} \times \vec{H}) - \Gamma_\perp \hat{S} \times \vec{H} + \Gamma_\perp \partial_t \hat{S}. \tag{1.11}$$

The effective LLG equation can be obtained by either eliminating the $\hat{S} \times (\hat{S} \times \vec{H})$ term or the $\hat{S} \times \partial_t \hat{S}$ term in Eqs. (1.10) and (1.11). If we eliminate the $\hat{S} \times \partial_t \hat{S}$ term by $(\beta N_{Mn} S + H_\parallel)\times$(1.10)- $\Gamma_\perp \times$(1.11), we obtain

$$\partial_t \hat{S} = (1 - \lambda)\hat{S} \times \vec{H} + \alpha_{pd} \hat{S} \times (\hat{S} \times \vec{H}), \tag{1.12}$$

where

$$\lambda = \frac{\beta s_{\parallel}(\beta N_{Mn} S + H_{\parallel})}{(\beta N_{Mn} S + H_{\parallel})^2 + \Gamma_{\perp}^2}, \tag{1.13}$$

and

$$\alpha_{pd} = \frac{\Gamma_{\perp} \beta s_{\parallel}}{(\beta N_{Mn} S + H_{\parallel})^2 + \Gamma_{\perp}^2} = \frac{s_{\parallel}}{N_{Mn} S} \frac{\Gamma_{\perp} h_{eff}}{(h_{eff} + H_{\parallel})^2 + \Gamma_{\perp}^2}, \tag{1.14}$$

where $h_{eff} = \beta N_{Mn} S$.

APPENDIX B

JONES FORMALISM

2.1 Jones Vectors

Consider an electromagnetic wave propagating along z-axis with an instantaneous $\vec{E}(t)$ vector. This can be represented by

$$\vec{E}(k,t) = \vec{e_x}E_x(k,t) + \vec{e_y}E_y(k,t). \tag{2.1}$$

If $E_\xi = E_{0\xi}e^{j(kz-\omega t+\phi_\xi)}(\xi = x, y)$, then

$$\vec{E}(k,t) = [\vec{e_x}E_{0x}e^{j\phi_x} + \vec{e_y}E_{0y}e^{j\phi_y}]e^{j(kz-\omega t)} = \tilde{E_0}e^{j(kz-\omega t)}, \tag{2.2}$$

where the term in brackets represents the complex amplitude of the plane wave, which can be written by a 2×1 matrix, or the so-called *Jones vector* as

$$\tilde{E_0} = \begin{pmatrix} \tilde{E_{0x}} \\ \tilde{E_{0y}} \end{pmatrix} = \begin{pmatrix} E_{0x}e^{j\phi_x} \\ E_{0y}e^{j\phi_y} \end{pmatrix}. \tag{2.3}$$

The state of the polarization of light is determined by the relative amplitudes (E_{0x}, E_{0y}), and the relative phases $(\delta = \phi_x - \phi_y)$. So Eq. (2.3) becomes

$$\tilde{E_0} = e^{j\phi_x}\begin{pmatrix} E_{0x} \\ E_{0y}e^{j\delta} \end{pmatrix}. \tag{2.4}$$

If the light is linearly polarized, and the electric field only oscillates along the x direction, the Jones vector is then written

$$\tilde{E_0} = \begin{pmatrix} E_{0x}e^{j\phi_x} \\ 0 \end{pmatrix} = \begin{pmatrix} A \\ 0 \end{pmatrix} = A\begin{pmatrix} 1 \\ 0 \end{pmatrix}, \tag{2.5}$$

where the phase ϕ_x is already set to zero for convenience. And similarly, for the light linearly polarized along y-axis with same intensity, the Jones vector has the form:

$$\tilde{E_0} = \begin{pmatrix} 0 \\ E_{0y}e^{j\phi_y} \end{pmatrix} = \begin{pmatrix} 0 \\ A \end{pmatrix} = A\begin{pmatrix} 0 \\ 1 \end{pmatrix}, \tag{2.6}$$

where the phase is also set to zero. With these results, we can obtain the Jones vector for linearly polarized light at any arbitrary angle α

$$\tilde{E}_0 = \begin{pmatrix} \tilde{E}_{0x} \\ \tilde{E}_{0y} \end{pmatrix} = A \begin{pmatrix} cos\alpha \\ sin\alpha \end{pmatrix}. \tag{2.7}$$

For circular polarized light, $E_{0x} = E_{0y}$. If we assume E_x leads E_y (counterclockwise rotation), then the Jones vector is written as

$$\tilde{E_0}^{(-)} = \begin{pmatrix} E_{0x}e^{j\phi_x} \\ E_{0y}e^{j\phi_y} \end{pmatrix} = A \begin{pmatrix} 1 \\ e^{j\pi/2} \end{pmatrix} = A \begin{pmatrix} 1 \\ j \end{pmatrix}, \tag{2.8}$$

where $A = 1/\sqrt{2}$ for the normalized form. The Eq.(2.8) represents the left-circularly polarized light. Correspondingly, the Jones vector $\tilde{E_0}^{(+)}$ for right-circularly polarized light can be obtained by replacing $\pi/2$ in Eq. (2.8) with $-\pi/2$. In general, for elliptically polarized light with $E_{0x} \neq E_{0y}$, the Jones vector can be written as

$$\tilde{E_0} = \begin{pmatrix} E_{0x} \\ E_{0y}e^{j\delta} \end{pmatrix}, \tag{2.9}$$

where $tan2\alpha = \frac{2E_{0x}E_{0y}cos\delta}{E_{0x}^2 - E_{0y}^2}$.

2.2 Jones Matrix

When light with a certain polarization passes through an optical element, its polarization state can be changed. Mathematically, this process can be regarded as applying a particular operation on the Jones vector. This operation may be represented by a 2×2 matrix, or the so-called *Jones matrix*. The elements often used in optical experiments are polarizers, half-wave plates and quarter-wave plates.

The Jones matrix for a linear polarizer with a transmission axis at θ is given by

$$M_{polarizer} = \begin{pmatrix} cos^2\theta & sin\theta cos\theta \\ sin\theta cos\theta & sin^2\theta \end{pmatrix}. \tag{2.10}$$

If the light passes through a phase retarder such as a half- or a quarter-wave plate, the Jones matrix will transform the elements in a Jones vector as follows

$$\begin{pmatrix} E_{0x}e^{j\phi_x} \Rightarrow E_{0x}e^{j(\phi_x+\varphi_x)} \\ E_{0y}e^{j\phi_y} \Rightarrow E_{0y}e^{j(\phi_y+\varphi_y)} \end{pmatrix},$$

where the transformation is represented by the matrix

$$M = \begin{pmatrix} e^{j\varphi_x} & 0 \\ 0 & e^{j\varphi_y} \end{pmatrix}.$$

For quarter- and half-wave plates, the phase difference $|\Delta\varphi|$ equals $\pi/2$ and π, respectively. If we assume $\varphi_y > \varphi_x$, the Jones matrices for quarter- and half-wave plates are shown as follows, respectively

$$M_{\lambda/4} = e^{-j\pi/4}\begin{pmatrix} 1 & 0 \\ 0 & j \end{pmatrix}, M_{\lambda/2} = e^{-j\pi/2}\begin{pmatrix} 1 & 0 \\ 0 & -1 \end{pmatrix}. \tag{2.11}$$

Another Jones matrix represents an E-vector oscillating linearly at α rotated by an angle Θ due to an optical element or a paricular physical mechanism,

$$M_{rot}(\Theta)\begin{pmatrix} cos\alpha \\ sin\alpha \end{pmatrix} = \begin{pmatrix} cos(\alpha+\Theta) \\ sin(\alpha+\Theta) \end{pmatrix}, \tag{2.12}$$

where

$$M_{rot}(\Theta) = \begin{pmatrix} cos\Theta & -sin\Theta \\ sin\Theta & cos\Theta \end{pmatrix}. \tag{2.13}$$

In this formulism, light propagates through a series of optical elements A_1,A_2,..., which can be represented by Jones matrices M_1,M_2,.... The incident $J^{(I)}$ and transmitted $J^{(T)}$ Jones vectors are then related by

$$J^{(T)} = M_N \cdots M_1 J^{(I)}. \tag{2.14}$$

2.3 Balanced Photodiodes

In our experiments, we employed a balanced photodiode scheme to measure the MOKE signal Θ_K $(=\theta_k + j\varepsilon_k)$, where θ_k and ε_k are Kerr rotation and ellipticity,

respectively. The polarization of the incident beam is rotated by the magnetized sample. A Wollaston prism, placed at $\pi/4$ with respect to the polarization direction of the incident beam, is placed in the reflected beam, and splits the beam into two beams with perpendicular polarizations and exactly equal intensities for the zero magnetization. The intensity difference, measured by the balanced photodiodes, becomes non-zero when the z component magnetization appears if probe beam is perpendicular to the sample.

If we assume a p-polarized incident beam represented by the Jones vector

$$J^{(I)} = \begin{pmatrix} 0 \\ 1 \end{pmatrix},$$

then the final Jones vector $J^{(T)}$ received by the detector can be calculated by Eq. (2.14)

$$J^{(T)} = \begin{pmatrix} E^s_{out} \\ E^p_{out} \end{pmatrix} = M_{rot}(\pi/4) M_{rot}(\Theta_K) J^{(I)} \approx -\frac{1}{\sqrt{2}} \begin{pmatrix} \Theta_K + 1 \\ \Theta_K - 1 \end{pmatrix}. \tag{2.15}$$

Therefore, the intensity difference ΔI is given by

$$\Delta I \propto |E^s_{out}|^2 - |E^p_{out}|^2 \approx \frac{1}{2}\{[(1+\theta_K)^2 + \varepsilon^2] - [(1-\theta_K)^2 + \varepsilon^2]\} = 2\theta_K. \tag{2.16}$$

Therefore, Eq. (2.16) demonstrates that it is possible to directly measure the Kerr rotation with the balanced photodiodes technique.

BIBLIOGRAPHY

[1] M.N.Baibich et al., Phys. Rev. Lett. **61**, 2472 (1988).

[2] G.Binasch, P.Grunberg, F.Saurenbach, and W.Zinn, Phys. Rev. B **39**, 4828 (1989).

[3] S. Wolf et al., Science **294**, 1488 (2001).

[4] D. Awschalom, D. Loss, and N. S. (eds.), *Semiconductor Spintronics and Quantum Computation*, Springer-Verlag, Berlin, 2002.

[5] I. Zutic, J. Fabian, and S. Sarma, Rev. Mod. Phys. **76**, 323 (2004).

[6] G. Prinz, Science **282**, 1660 (1998).

[7] J. Kikkawa and D. Awschalom, Phys. Rev. Lett. **80**, 4313 (1998).

[8] M. Oestreich et al., Semicond. Sci. Technol. **17**, 285 (2002).

[9] J. Kikkawa and D. Awschalom, Nature **397**, 139 (1999).

[10] I. Malajovich, J. Berry, N. Samarth, and D. Awschalom, Nature **411**, 770 (2001).

[11] I. Chuang, L. Vandersypen, X. Zhou, D. Leung, and S. Lloyd, Nature **393**, 143 (1998).

[12] G. Salis et al., Nature **414**, 619 (2003).

[13] Y. Kato et al., Science **299**, 1201 (2003).

[14] E. Beaureparie, J.-C. Merle, A. Daunois, and J.-Y. Bigot, Phys. Rev. Lett. **76**, 4250 (1996).

[15] J. Hohlfeld, E. Matthias, R. Knorren, and K. Bennemann, Phys. Rev. Lett. **78**, 4861 (1997).

[16] A. Scholl, L. Baumgarten, R. Jacquemin, and W. Eberhardt, Phys. Rev. Lett. **79**, 5146 (1997).

[17] G. Ju et al., Phys. Rev. Lett. **82**, 3708 (1999).

[18] B. Koopman, M. van Kampen, J. Kohlhepp, and W. de Jonge, Phys. Rev. Lett. **85**, 844 (2000).

[19] H. Rhie, H. Durr, and W. Eberhardt, Phys. Rev. Lett. **90**, 247201 (2003).

[20] T.Ogasawara et al., Phys. Rev. Lett. **94**, 087202 (2005).

[21] A. Kimel, A. Kirilyuk, A. Tsvetkov, R. Pisarev, and T. Rasing, Nature **429**, 850 (2004).

[22] A. Kimel et al., Nature **435**, 655 (2005).

[23] G. Ju et al., Phys. Rev. Lett. **93**, 197403 (2004).

[24] A. Kimel, A. Kirilyuk, F. Hansteen, R. Pisarev, and T. Rasing, J. Phys.: Condens. Matter **19**, 043201 (2007).

[25] Y. Ohno et al., Nature **402**, 790 (1999).

[26] H. Ohno et al., Nature **408**, 944 (2000).

[27] H. Ohno, Science **281**, 951 (1998).

[28] T. Jungwirth, J. Sinova, J. Masek, J. Kucera, and A. H. MacDonald, Rev. Mod. Phys **78**, 809 (2006).

[29] J. Qi et al., arXiv:0807.1740 (2008).

[30] J. Qi et al., Appl. Phys. Lett. **91**, 112506 (2007).

[31] J. Qi et al., Phys. Stat. Sol.(c) **5**, 2637 (2008).

[32] J. Qi et al., to be submitted .

[33] S. Colonna et al., Surface Science **601**, 4362 (2007).

[34] V. Kotov and A. Zvezdin, *Modern Magnetooptics and Magneto Optical Materials*, Institute of Physics, London, 1997.

[35] B. Koopmans, *Laser-Induced Magnetization Dynamics*, Springer, Berlin, 2004.

[36] M. Faraday, Experimental Researches in Electricity **3**, 2146 (1845).

[37] J. Kerr, Phil. Mag. **3**, 321 (1877).

[38] K. H. Bennemann, *Nonlinear Optics in Metals*, Oxford Science Publications, London, 1998.

[39] A. Kirilyuk, J. Phys. D: Apply. Phys. **35**, R187 (2002).

[40] B. Hillebrands and K. Ounadjela, *Spin Dynamics in Confined Magnetic Structures*, Springer-Verlag, Heidelberg, New York, 2002.

[41] T. Rasing, H. van den Berg, T. Gerrits, and J. Hohlfeld, *Ultrafast Magnetization and Switching Dynamics*, Springer, Berlin, 2004.

[42] J. Fassbender, *Magnetization Dynamics Investigated by Time-Resolved Kerr Effect Magnetometry*, Springer, Berlin, 2004.

[43] Y. Shen, *The Principles of Nonlinear Optics*, Benjamin, New York, 1984.

[44] R. Boyd, *Nonlinear Optics*, Academic, London, 1992.

[45] I. Sosnowska, T. Neumaier, and E. Steichela, J. Phys. C: Solid State Phys. **15**, 4835 (1982).

[46] R. Pan, H. Wei, and Y. Shen, Phys. Rev. B **39**, 1229 (1989).

[47] J. F. McGilp, L. Carroll, and K. Fleischer, Phys. Stat. Sol. (c) **5**, 2653 (2008).

[48] T. Kampfrath et al., Phys. Rev. B **65**, 104429 (2002).

[49] J. Bigot, L. Guidoni, E. Beaureparie, and P. Saeta, Phys. Rev. Lett. **93**, 077401 (2004).

[50] H. Ohno, J. Magn. Magn. Mat. **200**, 110 (1999).

[51] T. Story, R. Galazka, R. Frankel, and P. W. f, Phys. Rev. Lett. **56**, 777 (1986).

[52] T. Fukumura, H. Toyosaki, and Y. Yamada, Semicond. Sci. Technol. **20**, S103 (2005).

[53] M. Jamet et al., Naturre Materials **5**, 653 (2006).

[54] T. Dietl, Nature Materials **2**, 646 (2003).

[55] T. Dietl, H. Ohno, F. Matsukura, J. Cibert, and D. Ferrand, Science **287**, 1019 (2000).

[56] C. Kittel, *Introduction to Solid State Physics*, John Wiley & Sons, New York, 2004.

[57] E. Kane, J. Phys. Chem. Solids **1**, 249 (1957).

[58] R. Winkler, *Spin-Orbit Coupling Effects in Two-Dimentional Electron and Hole Systems*, Springer, Berlin, 2003.

[59] P. Y. Yu and M. Cardona, *Fundamentals of Semiconductors*, Springer-Verlag, Berlin, 2001.

[60] Y. Kato, *Electrical Manipulation of Electron Spin Coherence in Nonmagnetic Semiconductors*, Ph.d. dissertation, University of California, Santa Babara, 2005.

[61] R. Pierret, *Advanced Semiconductor Fundamentals*, Prentice Hall, New Jersey, 2003.

[62] Y. Oyama, J. Nishizawa, and K. Dezaki, J. Appl. Phys. **70**, 833 (1991).

[63] J. AgerIII, W. Walukiewicz, M. McCluskey, M. Plano, and M. I. Landstrass, Appl. Phys. Lett. **66**, 616 (1995).

[64] K. C. Ku et al., Appl. Phys. Lett. **82**, 2302 (2003).

[65] L. X. Zhao et al., Appl. Phys. Lett. **86**, 071902 (2005).

[66] J. Sadowski and J. Z. Domagala, Phys. Rev. B **69**, 075206 (2004).

[67] F. Matsukura, H. Ohno, A. Shen, and Y. Sugawara, Phys. Rev. B **57**, R2037 (1998).

[68] T. Dietl, H. Ohno, and F. Matsukura, Phys. Rev. B **63**, 195205 (2001).

[69] X. Liu, Y. Sasaki, and J. K. Furdyna, Phys. Rev. B **67**, 205204 (2003).

[70] S. Blundell, *Magnetism in Condensed Matter*, Oxford University Press, Oxford, 2001.

[71] C. Zener, Phys. Rev. **81**, 440 (1951).

[72] K. S. Burch et al., Phys. Rev. Lett. **97**, 087208 (2006).

[73] T. Jungwirth et al., Phys. Rev. B **76**, 125206 (2008).

[74] A. H. MacDonald, P. Schiffer, and N. Samarth, Nature Materials **4**, 195 (2005).

[75] R. A. Chapman and W. G. Hutchinson, Phys. Rev. Lett. **18**, 443 (1967).

[76] E. Kojima et al., Phys. Rev. B **68**, 193203 (2003).

[77] A. Kimel et al., Phys. Rev. Lett. **92**, 237203 (2004).

[78] Y. Mitsumori et al., Phys. Rev. B **69**, 033203 (2004).

[79] A. Oiwa, H. Takechi, and H. Munekata, Journal of Superconductivity **18**, 9 (2005).

[80] Y. Hashimoto, S. Kobayashi, and H. Munekata, Phys. Rev. Lett. **100**, 067202 (2008).

[81] A. Oiwa, Y. Mitsumori, R. Moriya, T. Slupinski, and H. Munekata, Phys. Rev. Lett. **88**, 137202 (2002).

[82] J. Wang et al., Phys. Rev. Lett. **98**, 217401 (2007).

[83] J. Chovan and I. E. Perakis, Phys. Rev. B **77**, 085321 (2008).

[84] L. D. Landau and E. M. Lifshitz, Phys. Z. Sowietunion **8**, 153 (1935).

[85] T. L. Gilbert, Phys. Rev. **100**, 1243 (1955).

[86] F. Bloch, Phys. Rev. **70**, 460 (1946).

[87] N. Bloembergen, Phys. Rev. **78**, 572 (1950).

[88] J. Shah, *Ultrafast Spectroscopy of Semiconductors and Semiconductor Nanostructures*, Springer, New York, 1999.

[89] J. G. Fujimoto, J. M. Liu, E. P. Ippon, and N. Bloembergen, Phys. Rev. Lett. **53**, 1837 (1984).

[90] D. Lim et al., Phys. Rev. B **71**, 134403 (2005).

[91] J. Wang et al., Phys. Rev. B **72**, 153311 (2005).

[92] P. S. Wu, J. Jun, J. Karpinski, J.-R. Park, and R. Sobolewski, Appl. Phys. Lett. **88**, 041917 (2006).

[93] C. Thomsen, H. T. Grahn, H. J. Maris, and J. Tauc, Phys. Rev. B **34**, 4129 (1986).

[94] H. J. Maris, *Physical Acoustics*, Academic, New York, 1971.

[95] J. Shah, Solid State Electron **21**, 43 (1978).

[96] M. Born, *Principles of Optics*, Cambridge University Press, New York, 1999.

[97] J. K. Miller et al., Phys. Rev. B **74**, 113313 (2006).

[98] M. dAquino, *Non-linear Magnetization Dynamics in Thin Films and Nanoparticles*, Ph.d. dissertation, University of Napoli, 2004.

[99] K. Lenz et al., Phys. Rev. B **73**, 144424 (2006).

[100] K. Hamaya et al., Phys. Rev. B **74**, 045201 (2006).

[101] W. Meiklejohn, Phys. Rev. **102**, 1413 (1956).

[102] J. Nogues and I. K. Schuller, J. Magn. Magn. Mater. **192**, 203 (1999).

[103] M. Kiwi, J. Magn. Magn. Matls **234**, 584 (2001).

[104] O. Wright, J. Appl. Phys. **71**, 1617 (1992).

[105] H.-Y. Hao and H. J. Maris, Phys. Rev. Lett. **84**, 5556 (2000).

[106] A. Devos et al., Phys. Rev. Lett. **98**, 207402 (2007).

[107] N. D. Lanzillotti-Kimura et al., Phys. Rev. Lett. **99**, 217405 (2007).

[108] Y. A. Burenkov, Y. M. Burdukov, S. Y. Davidov, and S. P. Nikanorov, Sov. Phys. Solid State **76**, 1175 (1973).

[109] H. Ohno et al., Appl. Phys. Lett. **69**, 363 (1996).

[110] J. S. Blakemore, J. Appl. Phys. **53**, R123 (1982).

[111] R. Aguado, M. P. Lopez-Sancho, J. Sinova, and L. Brey, Phys. Rev. B **70**, 195201 (2004).

[112] B. Koopmans, M. van Kampen, and W. J. M. de Jonge, J. Phys.:Condens. Matter **15**, S723 (2003).

[113] K. H. Bennemann, J. Phys.:Condens. Matter **16**, R995 (2004).

[114] J. Wang et al., J. Phys.:Condens. Matter **18**, R501 (2006).

[115] Y. Hashimoto, S. Kobayashi, and H. Munekata, Phys. Rev. Lett. **100**, 067202 (2008).

[116] E. Rozkotova et al., Appl. Phys. Lett. **92**, 122507 (2008).

[117] L. Cywinski and L. J. Sham, Phys. Rev. B **76**, 045205 (2007).

[118] J. Chovan, E. G. Kavousanaki, and I. E. Perakis, Phys. Rev. Lett. **96**, 057402 (2006).

[119] A. V. Kimel et al., Phys. Rev. B **62**, R10610 (2000).

[120] S. A. Crooker, J. J. Baumberg, F. Flack, N. Samarth, and D. D. Awschalom, Phys. Rev. Lett. **77**, 2814 (1996).

[121] D. J. Hilton and C. L. Tang, Phys. Rev. Lett. **89**, 146601 (2002).

[122] X. Liu, W. L. Lim, M. Dobrowolska, J. K. Furdyna, and T. Wojtowicz, Phys. Rev. B **71**, 035307 (2005).

[123] U. Welp, V. K. Vlasko-Vlasov, X. Liu, J. K. Furdyna, and T. Wojtowicz, Phys. Rev. Lett. **90**, 107201 (2003).

[124] E. J. Singley et al., Phys. Rev. B **68**, 165204 (2003).

[125] A. V. Kimel et al., Phys. Rev. Lett. **94**, 227203 (2004).

[126] J. Sinova et al., Phys. Rev. B **69**, 085209 (2004).

[127] Y. Tserkovnyak, G. A. Fiete, and B. I. Hlperin, Appl. Phys. Lett. **84**, 5234 (2004).

[128] M. Sparks, *Ferromagnetic Relaxation Theory*, Mc-Graw-Hill, New York, 1966.

[129] H. Suhl, IEEE Trans. Magn. **34**, 1834 (1998).

[130] M. Cartier, S. Auffret, Y. Samson, P. Bayle-Guillemaud, and B. Dieny, J. Magn. Magn. Mater. **63**, 223 (2001).

[131] S. Benedetti, P. Luches, M. Liberati, and S. Valeri, Surf. Sci. **572**, L348 (2004).

[132] T. Regan et al., Phys. Rev. B **64**, 214422 (2001).

[133] P. Luches et al., Phys. Rev. Lett. **96**, 106106 (2006).

[134] W. Roth, Phys. Rev. **111**, 772 (1958).

[135] G. A. Slack, J. Appl. Phys. **31**, 1571 (1960).

[136] S. Valeri, S. Benedetti, and P. Luches, J. Phys.: Condens. Matter **19**, 225002 (2007).

[137] J. F. Bobo et al., J. Magn. Magn. Mater. **206**, 118 (1999).

[138] G. Lupke, Surf. Sci. Rep. **35**, 75 (1999).

[139] G. McGilp, Prog. Surf. Sci. **49**, 1 (1995).

[140] H. Wierenga et al., Phys. Rev. Lett. **74**, 1462 (1995).

[141] S. Colonna, P. Luches, S. Valeri, and F. Boscherini, Nucl. Instrum. Methods Phys. Res. B **246**, 131 (2006).